

1 **In-situ estimation of soil hydraulic and hydrodispersive properties by**
2 **inversion of Electromagnetic Induction measurements and soil**
3 **hydrological modelling**

4 Giovanna Dragonetti^{1,Ψ}, Mohammad Farzamian^{2,3,Ψ}, Angelo Basile⁴, Fernando
5 Monteiro Santos³, Antonio Coppola⁵

6 ¹Mediterranean Agronomic Institute of Bari, Valenzano (BA), 70010, Italy

7 ²Instituto Nacional de Investigação Agrária e Veterinária, Oeiras, 2780-157, Portugal

8 ³Instituto Dom Luiz, Faculdade de Ciências da Universidade de Lisboa, Lisboa, 1749-016, Portugal

9 ⁴Institute for Mediterranean Agricultural and Forestry Systems, National Research Council, Portici (NA),
10 80055, Italy

11 ⁵School of Agricultural, Forestry, Food and Environmental Sciences, University of Basilicata, Potenza,
12 85100, Italy

13 **Ψ** These authors contributed equally to this work.

14 **Correspondence:** Mohammad Farzamian (mohammad.farzamian@iniav.pt) and Giovanna Dragonetti
15 (dragonetti@iamb.it)

16

17 **ABSTRACT**

18 Soil hydraulic and hydrodispersive properties are necessary for modelling water and solute
19 fluxes in agricultural and environmental systems. Despite the large efforts in developing methods
20 (e.g., lab-based, PTF), their characterization at applicative scales is still an imperative requirement.
21 Accordingly, this paper proposes a non-invasive in situ method integrating Electromagnetic
22 Induction (EMI) and hydrological modelling to estimate soil hydraulic and transport properties at
23 the plot scale. To this aim, we carried out two sequential water infiltration and solute transport
24 experiments and conducted time-lapse EMI surveys using a CMD mini-Explorer to examine how
25 well this methodology can be used to i) monitor water content dynamic after irrigation and to

26 estimate the soil hydraulic van Genuchten–Mualem parameters from the water infiltration
27 experiment and ii) to monitor solute concentration, and to estimate solute dispersivity from the
28 solute transport experiment. We then compared the obtained results to those estimated by direct
29 TDR and tensiometer probes measurements. Our results show a good agreement between EMI-
30 based estimation of soil hydraulic and transport properties with those obtained from the direct TDR
31 and tensiometer probes measurements. When compared with direct TDR measurements, the EMI
32 significantly underestimated the water content distribution, but the water content evolved similarly
33 over time. This did not have a significant impact on the hydraulic conductivity curves since the
34 hydraulic conductivity is mainly a function of water content variation, not its absolute value. On
35 the other hand, this underestimation led to lower saturated water content, reflected in the water
36 retention curve. The latter can be scaled by measuring the actual saturated water content at the end
37 of the experiment with TDR probes or even by weighing soil samples.

38

39 **1. INTRODUCTION**

40 Dynamics agro-hydrological models are more and more used for interpreting and solving agro-
41 environmental problems (Hansen et al., 2012; Coppola et al., 2015; Kroes et al., 2017; Coppola et
42 al., 2019). The soil hydrological component of these models is frequently based on mechanistic
43 descriptions of water and solute fluxes in soils. Richards equation (RE) for water flow and
44 Advection-Dispersion equation (ADE) for solute transport is generally accepted to apply at a local
45 scale (plot scale, for example). Solving RE requires the determination of the hydraulic properties,
46 namely the water retention curve relating the soil water content, θ , to the soil water pressure head,
47 h , and the hydraulic conductivity curve, relating the hydraulic conductivity, K to either the water
48 content, θ or the pressure head, h . Similarly, ADE requires the dispersivity, λ , to be also known.

49 In the last decades several laboratory and in-situ methods have been developed for characterizing
50 soil hydraulic properties (e.g. Dane and Topp, 2020) and dispersive properties (e.g. Vanderborght
51 and Vereecken, 2007). Lab-based characterizations may be carried out under more controlled
52 conditions. Nevertheless, for simulating water and solute dynamics in the real field context, the in-
53 situ methods are obviously more representative than the lab ones. This is firstly related to the size
54 of the volume investigated, which has to appropriately represent the heterogeneity of the medium
55 being studied (Wessolek et al., 1994; Ellsworth et al., 1996; van Genuchten et al., 1999; Inoue et
56 al., 2000). Actually, a water flow process observed in situ will be influenced by the heterogeneities
57 (stones, macropores, etc.) found in the field. This is the main limitation of the relatively small soil
58 columns generally analysed in the laboratory. By contrast, an in-situ characterization method, for
59 example the well-known instantaneous profile method (Watson et al., 1966), can catch the
60 hydraulic properties which are effective in describing the flow process observed in-situ. This will
61 also depend on the measurement scale (the size of the plot) and on the observation scale of the
62 sensors used. These issues have been dealt with in detail for example in Coppola et al. (2012;
63 2016) and in Dragonetti et al., (2018). Besides, the experimental boundary conditions used to carry
64 out the hydraulic characterization in lab and in-situ may also induce a different shape of the
65 hydraulic properties as determined in the lab and in-situ (Basile et al., 2006).

66 In-situ methods typically evaluate soil hydraulic properties by monitoring an infiltration and/or
67 a redistribution water flow process (Watson et al., 1966). Similarly, in situ methods for
68 determining hydro-dispersive parameters are generally based on monitoring of mixing processes
69 following pulse or step inputs of a tracer on either large plots or along field transect (Severino et
70 al., 2010; Coppola et al., 2011; Vanderborght and Vereecken, 2007). Inverse modelling is
71 frequently used to estimate the hydraulic and transport parameters simultaneously (Šimůnek et al.,

72 1998; Abbasi et al., 2003; Groh et al., 2018). Yet, even by shortening the measurement procedure
73 by simplified assumptions (e.g., Sisson and van Genuchten 1991; Basile 2006) all in-situ methods
74 for the characterization of the whole soil profile remain extremely difficult to implement also
75 because they generally require installing sensors at different depths (e.g. TDR probes,
76 tensiometers, access tubes for neutron probe) which are cumbersome and may induce soil
77 disturbance, unless the installation is made much earlier than the experiment, to at least partly
78 allowing the soil to recover through several wetting-drying cycles its natural structure.

79 In this direction, geophysical non-invasive methods based on the electrical resistivity
80 tomography (ERT) and Electromagnetic Induction (EMI) techniques represent a promising
81 alternative to traditional sensors for soil hydraulic and transport parameters assessment. Many
82 researchers have used the time-lapse ERT data (Binley et al., 2002; Kemna et al., 2002; Singha
83 and Gorelick, 2005) to monitor temporal water content and solute concentration changes in flow
84 and transport models. The dependence of soil electrical conductivity on soil water content and
85 concentration is the key mechanism that permits the use of time-lapse ERT to monitor water and
86 solute dynamics in time-lapse mode along a soil profile, by relating resistivities to water contents
87 and solute concentration distributions through empirical or semi-empirical relationships (e.g.
88 Archie, 1942) or established in-situ relationships (e.g. Binley et al., 2002).

89 Electromagnetic induction (EMI) sensors may be used as an alternative to the ERT technique
90 as they allow for monitoring water and solute propagation through a soil profile by simply moving
91 the sensor above the soil surface without the need to install electrodes. An EMI sensor provides
92 measurements of the depth-weighted apparent electrical conductivity (σ_a) according to the specific
93 distribution of the bulk electrical conductivity (σ_b), as well as the depth response function of the
94 sensor used (McNeill, 1980). σ_a obtained from EMI sensors have been used to map the geospatial

95 and temporal variability of the soil water content and salinity (Corwin and Lesch, 2005; Bouksila
96 et al. 2012; Saeed et al., 2017). However, monitoring the propagation of the water and solutes with
97 depth along a soil profile (as during a water infiltration or a solute transport experiment) requires
98 the distribution of the σ_b distribution with depth to be known over time, which can be obtained by
99 inversion of the σ_a observations from the EMI sensor (see for example, Borchers et al., 1997;
100 Hendrickx et al., 2002; Lavoué et al., 2010; Mester et al., 2011; Deidda et al., 2014; Von Hebel et
101 al., 2014; Dragonetti et al., 2018; Moghadas et al., 2019; Farzamian et al., 2019a; Zare et al. 2020;
102 Mclachlan et al. 2020). More recently, this inversion has been facilitated by the development of
103 multi-coil EM sensors which are designed to collect σ_a at multiple coil spacing and orientations
104 simultaneously in one sensor reading. This allows a rapid investigation of the soil's electrical
105 conductivity at several depth ranges to obtain soil water content (Huang et al., 2016; Whalley et
106 al., 2017) and solute concentrations (Paz et al., 2020; Gomez Flores et al., 2022) quickly and
107 cheaply. However, the potential of EMI sensors to assess soil hydraulic and hydro-dispersive
108 parameters has not been yet studied due to the lack of high-resolution and well-controlled
109 experiments, required to catch the complexity of water flow and transport process during
110 infiltration experiments.

111 With these premises, in this paper we propose a procedure based on a sequence of water
112 infiltration and solute transport experiments, both monitored by an EMI sensor, with the objective
113 of estimating in-situ the parameters of soil hydraulic properties and the dispersivity of a soil profile
114 with a non-invasive EMI sensor and relatively short experiments at the plot scale. The sequence
115 of water and solute infiltration has the main aim to discriminate the contribution of the water
116 content and the soil solution electrical conductivity to the EMI-based σ_b . All the EMI data will be
117 analysed by a hydrological model within a so-called uncoupled framework, which will be

118 discussed in detail in the *Hydro-Geophysical uncoupled approach* section. The goodness of the
119 adopted approach will be evaluated by comparing the EMI-based hydraulic and hydrodispersive
120 properties to those obtained from in-situ TDR and tensiometer measurements. Our aim is to
121 explore an approach that doesn't need sensors installation and minimise data necessary for the in-
122 situ assessment of soil hydraulic and hydrodispersive properties.

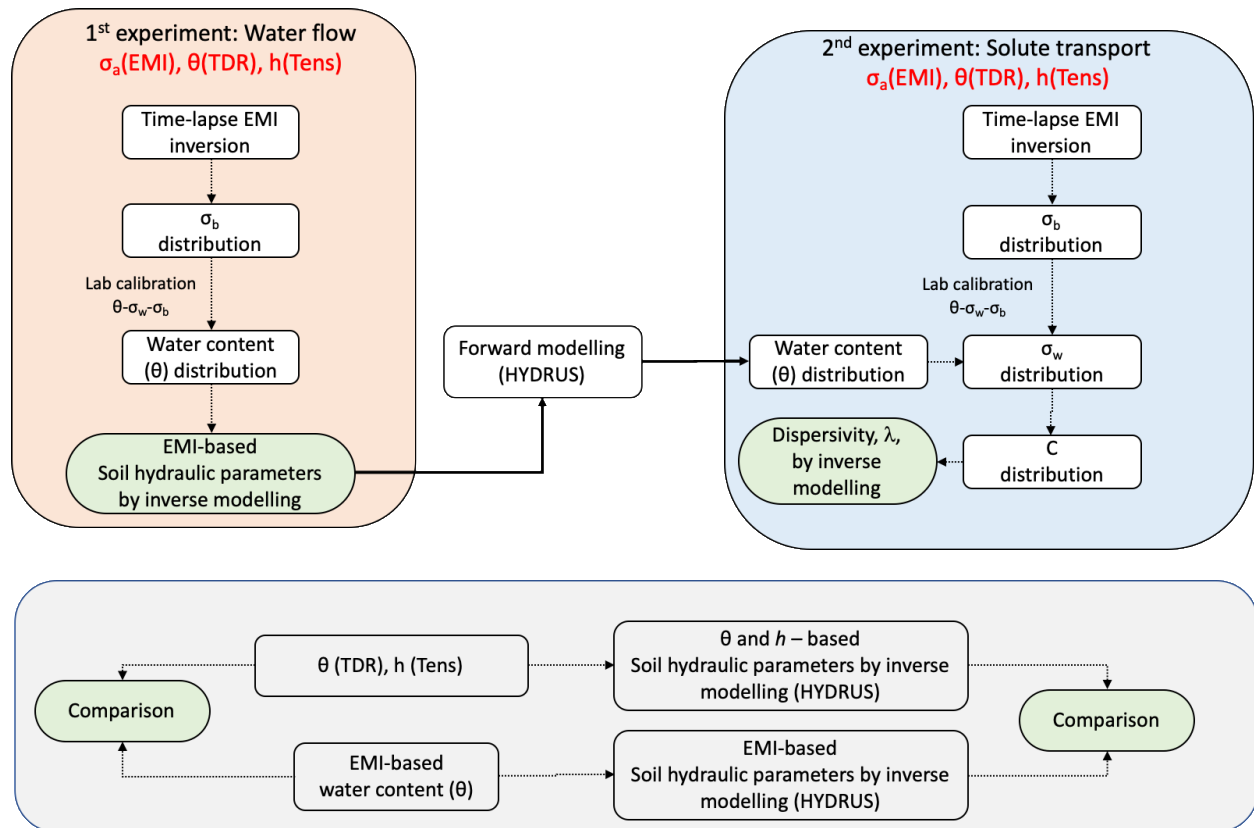
123

124 **2. HYDRO-GEOPHYSICAL UNCOUPLED APPROACH**

125 Figure 1 provides a schematic view of a six-step (+ one step for comparison) procedure, based
126 on an uncoupled approach (Camporese et al., 2015) which will be adopted in this work to estimate
127 the soil hydraulic and hydrodispersive properties using the data obtained from the EMI sensor. All
128 the steps summarised below will be described in detail in the Materials and Methods section.

- 129 (i) Inversion of time-lapse σ_a EMI data obtained during (i) a water infiltration experiment,
130 hereafter 1st experiment, and (ii) a subsequent solute transport experiment, hereafter 2nd
131 experiment, to generate EMI-based σ_b distributions for each experiment;
- 132 (ii) Laboratory calibration of the relationship θ - σ_b - σ_w in order to convert σ_b distributions to water
133 content, θ , (1st experiment) and to soil solution electrical conductivity, σ_w , and therefore
134 solute concentrations, C , (2nd experiment);
- 135 (iii) Converting the σ_b distributions obtained from the 1st experiment to water content
136 distributions, using the θ - σ_b - σ_w relationship, to be used in the next numerical simulation step;
- 137 (iv) Numerical simulation, by using the HYDRUS-1D model (Šimůnek et al., 1998), of the 1st
138 experiment in order to estimate the van Genuchten-Mualem (vG-M) parameters through an
139 inversion procedure based on the water contents inferred from step (iii);

- 140 (v) Conversion of the σ_b distributions obtained from the 2nd experiment to solute concentration
141 distribution in order to estimate longitudinal dispersivity, λ . In this step, σ_w distribution was
142 estimated by using the laboratory θ - σ_b - σ_w calibration. The θ distribution in the 2nd
143 experiment was simulated based on the vG-M parameters obtained in step (iv). This is a
144 crucial step in the proposed procedure, as it allows to discriminate the contribution of the
145 soil water electrical conductivity, and thus of the solute concentration, to the σ_b EMI readings
146 during the 2nd experiment. The σ_w distributions were thus converted to solute concentration
147 by a simple standard lab-based solute specific σ_w - C relationship;
- 148 (vi) Numerical simulation of the second solute infiltration process in order to estimate λ through
149 an inversion procedure based on the concentrations obtained from step (v).
- 150 (vii) An alternative dataset of θ and σ_b obtained from direct TDR measurements, as well as
151 tensiometer pressure head (h) readings, collected during the two experiments, allowed us to
152 obtain independent hydraulic and hydrodispersive properties (hereafter TDR-based for sake
153 of simplicity) to be used as a reference to evaluate the EMI-based parameter estimation (see
154 the horizontal grey box in Fig. 1).



155

156 Figure 1: Schematic diagram of the proposed Hydro-Geophysical uncoupled approach

157

158 3. MATERIAL AND METHODS

159 3.1. Study area

160 The experiment was performed at the Mediterranean Agronomic Institute of Bari (CIHEAM-

161 IAM), south-eastern coast of Italy. The study area is located at an altitude of 72 m with $41^\circ 3'$

162 $13.251''$ N, a longitude of $16^\circ 52' 36.274''$ E, and an elevation of about 68 m a.s.l. with a typical

163 Mediterranean climate with rainy winters and very hot dry summers. The soil is a Colluvic Regosol

164 consisting of silty loam layers of an average depth of 70 cm on a shallow fractured calcareous

165 rock. Two main horizons on the calcareous rock may be identified: an Ap horizon (depth 0-30 cm)

166 and a Bw horizon (depth 30-70 cm). Scattered calcareous fragments are present due to the breaking

167 and grinding of the bedrock operated in the past by using heavy machinery in order to improve the
168 soil structure and increase the soil depth for plantation

169 **3.2. Experimental set-up**

170 A layout of the experimental setup is shown in Fig. 2. The plot size is 4×4 m. Water was
171 applied by using a drip irrigation system consisting of 20 lines, with drippers spaced 0.20 m and
172 delivering a nominal flow rate of 10 l h^{-1} . Thus 400 drippers were installed, capable of delivering
173 4000 l h^{-1} on the whole plot. The dripper's grid spacing and the flow rate were selected to ensure
174 that a 1D flow field rapidly developed after starting irrigation. The drip irrigation system was
175 placed on a metallic grid to be easily moved away from the plot and whenever EMI measurements
176 were taken on the ground soil.

177 Several months before starting the 1st experiment, after digging a small pit, eight three-wire
178 TDR probes, 7 cm long, 2.5 cm internal distance, and 0.3 cm in diameter, were inserted
179 horizontally at 2 depths – 20 and 40 cm, corresponding to the Ap and the Bw horizon – in the 4
180 corners of the experimental plot (at 1 m distance from the plot edge), as shown in Fig. 2. The pits
181 for installing the sensors were refilled immediately, to leave some natural wetting and drying
182 cycles to reproduce the original soil aggregation. Then, the plot was covered with a plastic sheet
183 about four days prior to the start of the experiment to keep the plot under quasi-equilibrium
184 conditions at the beginning of the experiment.

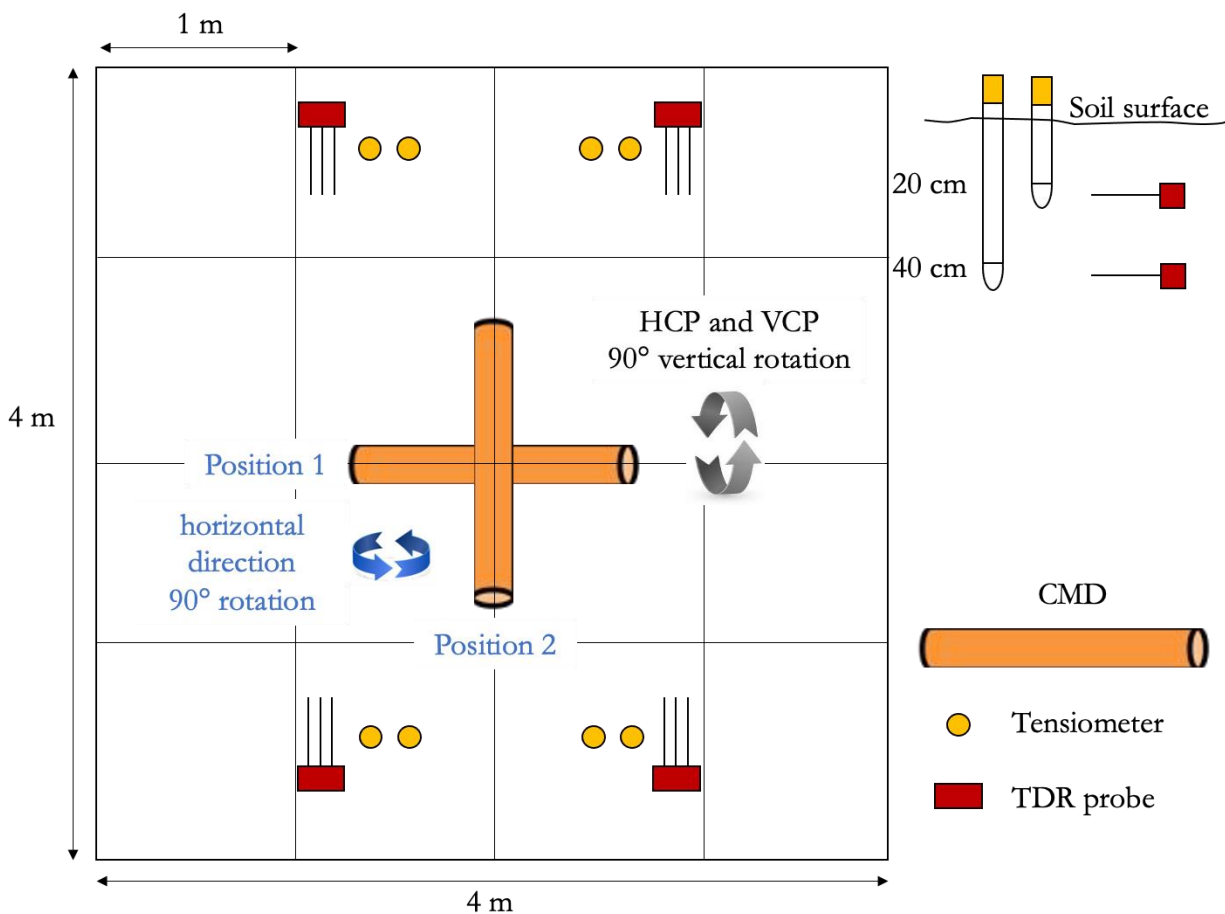
185 A Tektronix 1502C cable tester (Tektronix Inc., Baveron, OR) was used in this study, enabling
186 simultaneous measurement of water content, θ , and bulk electrical conductivity, σ_b , of the soil
187 volume explored by the probe (Robinson et al., 2003; Coppola et al., 2011; 2013). Furthermore,
188 eight tensiometers were vertically inserted near each TDR probe to acquire water potentials by a

189 Tensicorder sensor (Hydrosense3 SK800). Both TDR probes and tensiometers were installed for
190 the evaluation of the EMI-based parameter estimation (step (vii)).

191 The experimental plot was firstly irrigated by using tap water with an electrical conductivity
192 of about 1 dS m⁻¹ (1st experiment). We applied eleven irrigations, each lasting about 3 minutes to
193 deliver about 180 l on the whole 16 m² plot for each irrigation (the volume was measured by a
194 flowmeter). Irrigations were separated by about a 1-hour shutoff. At each irrigation starting, due
195 to the short inertia of the irrigation system just after its switching on, for some seconds drippers
196 delivered less than 10 l h⁻¹. For each irrigation an average flow rate of about 0.375 cm min⁻¹ was
197 applied, which generated a small ponding at the soil surface for a short time. Overall, an average
198 water volume of 2000 l was supplied.

199 The propagation of the wetting front along the soil profile was monitored by using an EMI
200 sensor (i.e. CMD mini-Explorer, GF Instruments, Czech Republic), positioned horizontally in the
201 middle of the plot (Fig. 2) in order to measure the apparent electrical conductivity, σ_a , in the soil
202 profile in VCP (vertical coplanar, i.e., horizontal magnetic dipole configuration) mode and then
203 HCP (horizontal coplanar, i.e., vertical magnetic dipole configurations) mode by rotating the probe
204 90° axially to change the orientation from VCP to HCP mode. The CMD Mini-Explorer operates
205 at 30 kHz frequency and has three receiver coils with 0.32, 0.71 and 1.18 m distances from the
206 transmitter coil, referred to hereafter as ρ_{32} , ρ_{71} , and ρ_{118} . The manufacturer indicates that the
207 instrument has an effective depth range of 0.5, 1.0 and 1.8 m in the HCP mode, which is reduced
208 to half (0.25, 0.5, and 0.9 m) by using the VCP orientation. As a consequence, this EMI sensor
209 returns six different σ_a values (utilizing three offsets with two coil orientations) with each
210 corresponding to different depth sensitivity ranges. All measurements were performed five
211 minutes after each water pulse application by temporarily removing the irrigation grid and placing

212 the EMI sensor in the middle of the plot. The infiltration was also monitored by TDR probes and
 213 tensiometers in order to monitor the space-time evolution of water content, θ , pressure head, h , as
 214 well as bulk electrical conductivity, σ_b . The distance of the TDR probes and tensiometers to the
 215 middle of the plot was specifically designed to avoid any interference with the EMI measurements.



216
 217 Figure 2. Layout of the experimental and monitoring set-up. HCP (horizontal coplanar) and VCP
 218 (vertical coplanar) are the vertical and horizontal dipolar orientations of the CMD probes,
 219 respectively.

220
 221 At the end of the 1st experiment, the soil was allowed to dry and then covered with a plastic
 222 sheet to bring the distribution of water content along the profile similar to the initial one (observed

223 before the water infiltration test). Afterward, a similar infiltration experiment (2nd) was carried out
 224 but using saline water at an electrical conductivity of 15 dS m⁻¹, and obtained by mixing CaCl₂
 225 into the tap water. Again, eleven saline water supplies were provided at intervals of about 1 h apart
 226 and a total volume of 2000 l saline water was supplied during the experiment. The propagation of
 227 the water and chloride during the 2nd infiltration experiment was monitored similarly to the 1st
 228 experiment using TDR probes, tensiometers, and the CMD Mini-Explorer sensor.

229 **3.3. Site-specific calibration θ - σ_b - σ_w**

230 The relationship between the bulk electrical conductivity (σ_b), the electrical conductivity of the
 231 soil solution soil water (σ_w), and the water content, were obtained by using the model proposed by
 232 Malicki and Walczak, (1999):

$$233 \sigma_w = \frac{\sigma_b - a}{(\varepsilon_b - b)(0.0057 + 0.000071 S)} \quad (1)$$

234 where ε_b (-) is the dielectric constant, which is related to the water content and S is the sand content
 235 in percent. The parameters $a = 3.6$ dS m⁻¹ and $b = 0.11$ were obtained in a laboratory experiment
 236 reported in Farzamian et al. (2021). The lab experiment for such a calibration is quite simple, fast,
 237 and standard procedure on reconstructed soil samples. An additional linear calibration, obtained
 238 by using solutions at different concentrations of calcium chloride was used to relate soil water
 239 concentrations of chloride, Cl⁻, to σ_w .

240 **3.4. Inversion of time-lapse EMI σ_a data**

241 Time-lapse σ_a data obtained during the experiments were inverted using a modified inversion
 242 algorithm proposed by Monteiro Santos et al. (2004) to obtain σ_b distribution in time. The aim of
 243 the inversion is to minimize the penalty function that consists of a combination between the
 244 observations' misfit and the model roughness (Farzamian et al., 2019b). The earth model used
 245 in the inversion process consists of a set of 1D models distributed according to the number of time-

246 lapse measurements. All the models have the same number of layers (i.e. 7) whose thickness is
 247 kept constant. The selected thickness of layers is 10, 20, 30, 40, 55, 75 and 180 cm. The number
 248 and thickness of layers were selected based on several factors including the number of σ_a
 249 measurements (i.e., 6), effective depth range of HCP and VCP modes (i.e., 5 of 6 measurements
 250 have an effective depth of less than 1m), and site specifications (i.e., the large variability of
 251 conductivity of the soil profile over a resistive bedrock). The parameters of each model are
 252 spatially and temporally constrained using their neighbours through smooth conditions. The
 253 forward modelling is solved based on the full solution of the Maxwell equations (Kaufman and
 254 Keller, 1983) to calculate the σ_a responses of the model. The inversion algorithm is Occam-
 255 regularization and the objective function was developed based on Sasaki, (2001). Therefore, the
 256 corrections of the parameters, in an iterative process are calculated solving the system:

$$257 \quad [(J^T J + \eta C^T C)] \delta p = J^T b \quad (2)$$

258 where δp is the vector containing the corrections applied to the parameters (logarithm of
 259 block conductivities, p_j) of an initial model, b is the vector of the differences between the logarithm
 260 of the observed and calculated σ_a [$b_i = \ln(\sigma_a^o/\sigma_a^c)_i$], J is the Jacobian matrix whose elements are
 261 given by $(\sigma_j/\sigma_{ai}^c) (\partial\sigma_{ai}^c/\partial\sigma_j)$, the superscript T denotes the transpose operation, and η is a Lagrange
 262 multiplier that controls the amplitude of the parameter corrections and whose best value is
 263 determined empirically. The elements of matrix C are the coefficients of the values of the
 264 roughness of each 1D model, which is defined in terms of the two neighbour's parameters and the
 265 constraint between the parameters of the different models on time. In this regard and in our
 266 temporal 1D experiment, each cell is constrained spatially by its vertical neighbours, while the
 267 temporal constraints are imposed using its lateral neighbours. An iterative process allows the final
 268 models to be obtained, with their response fitting the data set in a least-square sense. In terms of

269 η , generally, large values will produce smooth inversion results with smoother spatial and temporal
270 variations.

271 We performed several synthetic tests to determine how well the proposed inversion algorithm
272 can predict spatiotemporal variability of σ_b and to fine-tune the regularization parameters. The
273 synthetic scenarios were selected based on spatiotemporal variability of σ_a in the HCP and VCP
274 modes, the site specification (e.g., shallow bedrock) and the expected evolution of conductive zone
275 due to water and saline water infiltrations.

276 **3.5. Numerical simulation of water flow and chloride transport in soil**

277 The water and the chloride propagation monitored during the experiments were simulated by
278 using the HYDRUS-1D model (Šimůnek et al., 1998). HYDRUS-1D simulates water flow and
279 solute transport by solving the Richards equation and the Advection-Dispersion equation,
280 respectively.

281 Richards equation can be written for one-dimensional, unsaturated, non-steady state flow of
282 water in the vertical direction as follows:

$$283 \quad C_w(\theta) \frac{\partial h}{\partial t} = \frac{\partial}{\partial z} \left[K(h) \frac{\partial h}{\partial z} + K(h) \right] \quad (3)$$

284 where $C_w(\theta)$, the water capacity, is the slope of the water retention curve, θ is the volumetric water
285 content [L^3L^{-3}], h is the soil water pressure head [L], $K(h)$ is the unsaturated hydraulic conductivity
286 [LT^{-1}].

287 The Advection-Dispersion equation governing the transport of a single non-reactive and non-
288 adsorbed (a tracer, chloride in our case) ion in the soil can be written as:

$$289 \quad \frac{\partial(\theta C)}{\partial t} = \frac{\partial}{\partial z} \left[\theta D \frac{\partial C}{\partial z} - qC \right] \quad (4)$$

290 where q is the darcian flux, C is the solute concentration in the liquid phase [ML^{-3}], D (L^2T^{-1}) is
 291 the effective dispersion coefficient, which can be assumed to come from a combination of the
 292 molecular diffusion coefficient, D_{diff} (L^2T^{-1}) and the hydrodynamic dispersion coefficient, D_{dis}
 293 (L^2T^{-1}):

$$294 \quad D = D_{\text{diff}} + D_{\text{dis}} \quad (5)$$

295 where hydrodynamic dispersion is the mixing or spreading of the solute during transport due to
 296 differences in velocities within a pore and between pores. The dispersion coefficient can be related
 297 to the average pore water velocity $v=q/\theta$ through:

$$298 \quad D = \lambda v \quad (6)$$

299 where λ [L] is the dispersivity, a characteristic property of the porous medium. To solve the
 300 Richards equation (Eq. 3), the water retention function, $\theta(h)$, and the hydraulic conductivity
 301 function, $K(h)$, must be defined. In this paper we adopted the van Genuchten-Mualem model (vG-
 302 M), (Van Genuchten, 1980):

$$303 \quad S_e = [1 + (\alpha|h|)^n]^{-m} \quad (7)$$

$$304 \quad K(h) = K_s S_e^\tau \left[1 - (1 - S_e^{1/m})^m \right]^2 \quad (8)$$

305 In Eqs. 7 and 8, $S_e = \frac{(\theta - \theta_r)}{(\theta_s - \theta_r)}$ is the effective water saturation, θ_s the saturated water content, θ_r the
 306 residual water content, α , n and m are fitting parameters with m taken as $m=1-1/n$, K_s is the
 307 saturated hydraulic conductivity and τ is the pore-connectivity parameter.

308

309 **3.6. Inverse estimation of soil hydraulic and solute transport parameters**

310 The obtained EMI-based spatiotemporal distribution of σ_b during the 1st experiment was
311 converted to the θ distribution in order to estimate the temporal evolution of θ during the
312 infiltration process. These water content data were then used in an optimization procedure by using
313 the HYDRUS-1D model, in order to estimate the hydraulic properties of the different horizons in
314 the soil profile. The simulations were carried out by using the actual top boundary flux conditions
315 during the experiment, including the irrigation events. For the bottom boundary, free drainage was
316 considered. A simulation domain of 150 cm depth was considered. The same procedure was
317 repeated using the direct measurements of θ and h inferred from TDR and tensiometers,
318 respectively, in order to obtain independent hydraulic parameters (TDR-based estimation) to be
319 compared to those inferred from EMI. A three-layer soil profile (0-25; 25-70; 70-150 cm),
320 reflecting the actual pedological layering (i.e. Ap, Bw, and bedrock) was used in all simulations.
321 In terms of the initial condition, a hydrostatic distribution of the pressure heads, h , was considered
322 for the TDR-based simulations. On the other hand, the water content distribution, inferred from
323 the first EMI survey (before irrigation) was considered for the EMI-based simulation.

324 As for the solute transport experiment, a HYDRUS-1D simulation was carried out with the
325 EMI-based hydraulic properties obtained from the 1st experiment to simulate the water content
326 distributions in correspondence with the EMI measurement times. The simulations of water
327 infiltration and solute transport in the 2nd experiment were carried out by using the top boundary
328 fluxes conditions applied during the 2nd experiment along with the same simulation domain, three-
329 layer soil profile, and the bottom boundary and equilibrium initial conditions described above.
330 Thus, for each monitoring time, we had available the σ_b distributions obtained from the EMI and
331 the θ distributions coming from the HYDRUS-1D simulations. These distributions allowed us to
332 estimate as many σ_w (and thus C) distributions by using the θ - σ_b - σ_w relationship obtained in the

333 laboratory. These C distributions were used in a new HYDRUS-1D simulation to estimate the
334 longitudinal dispersivity of the investigated soil. The simulated concentrations, with the optimized
335 dispersivity, λ , were compared to those obtained from the TDR and tensiometer data.

336

337 **4. RESULTS AND DISCUSSION**

338 **4.1. Water infiltration – 1st experiment**

339 *4.1.1. Time-lapse σ_a data and estimation of σ_b distribution*

340 Figure 3 shows the σ_a values observed during the water infiltration experiment. Both VCP
341 and HCP modes show a relatively similar pattern of σ_a values with $\rho32$ and $\rho118$ being the highest
342 and lowest respectively. HCP mode shows higher values compared to the VCP mode in the same
343 receivers. This pattern of σ_a distribution suggests the presence of a conductive zone over a resistive
344 zone which is expected in this experiment as a result of the waterfront being infiltrated into the
345 soil profile and the presence of a resistive bedrock. In terms of temporal σ_a variabilities, the σ_a
346 increases consistently in both VCP and HCP modes during the first three hours of the experiment.
347 Afterward, σ_a did not change significantly toward the end of the experiment. The range of σ_a
348 variations is relatively small in both VCP and HCP modes with the former in the 10-30 mS m⁻¹
349 range and the latter in the 10-50 mS m⁻¹ range.

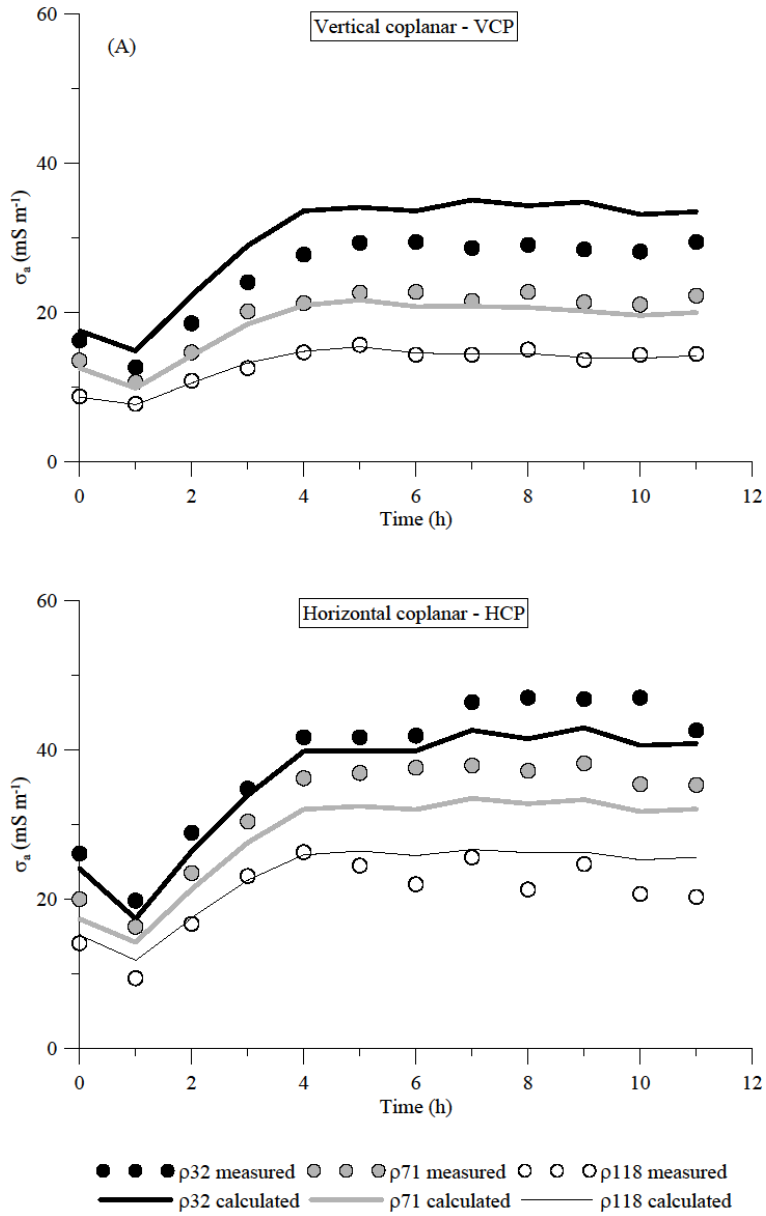
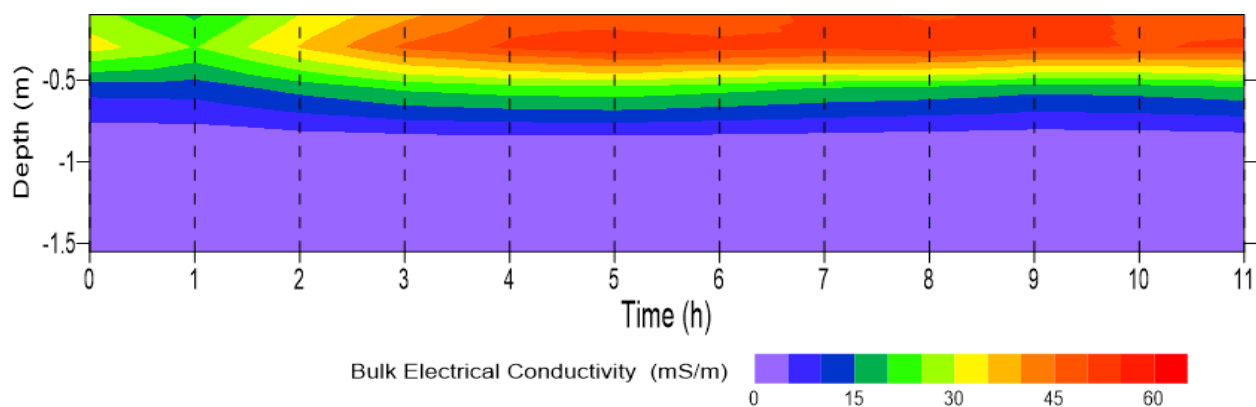


Figure 3: σ_a values observed during the water infiltration experiment. (A) VCP, (B) HCP. The symbols represent the measured data whereas the lines represent the values calculated after the inversion.

350 Prior to the inversion of σ_a data we fine-tuned the regularization parameter, η , as discussed
 351 in 3.4. the results of several synthetic tests (not shown here) suggest that a value of η between 1 to

352 5 provides a better result in resolving the spatio-temporal σ_b distributions in both experiments.
 353 Figure 4 depicts the time-lapse σ_b modelling results of σ_a shown in Fig. 3. The model shows clearly
 354 the evolution of the conductive zone into the soil profile shortly after the irrigation started as
 355 expected from the σ_a data. The resistive zone beneath a conductive zone corresponds to the bedrock
 356 layer in the experimental plot. The σ_b of the resistive zone remains below 5 mS m^{-1} and does not
 357 vary significantly during the experiment, while, in contrast, the σ_b of the upper layers increased
 358 significantly from an average of 20 mS m^{-1} at the beginning of the experiment to more than 50 mS
 359 m^{-1} after the 5th irrigation. The conductivity of this zone does not increase largely since then,
 360 suggesting that the upper soil is fairly saturated after the 5th irrigation. The calculated response of
 361 this model was shown in Fig. 3. There is a fairly good agreement between σ_a measurements and
 362 model response, however, a slight shift can be noticed in the ρ_{32} - VCP mode and ρ_{71} - HCP mode
 363 between data and model response. This shift can be due to several reasons such as i) the
 364 instrumental shift of one or more channels, ii) the large spatiotemporal variability of soil electrical
 365 conductivity in this experiment as well as smoothness constraint performed in the inversion
 366 process to stabilize the inversion process which make it difficult to resolve the sharp changes, and
 367 iii) the choice of initial model.



368
 369 Figure 4. Time evolution of bulk electrical conductivity (σ_b) distribution with depth during the
 370 water infiltration experiment.

4.1.2. Comparison between TDR-based and EMI-based σ_b and θ distributions

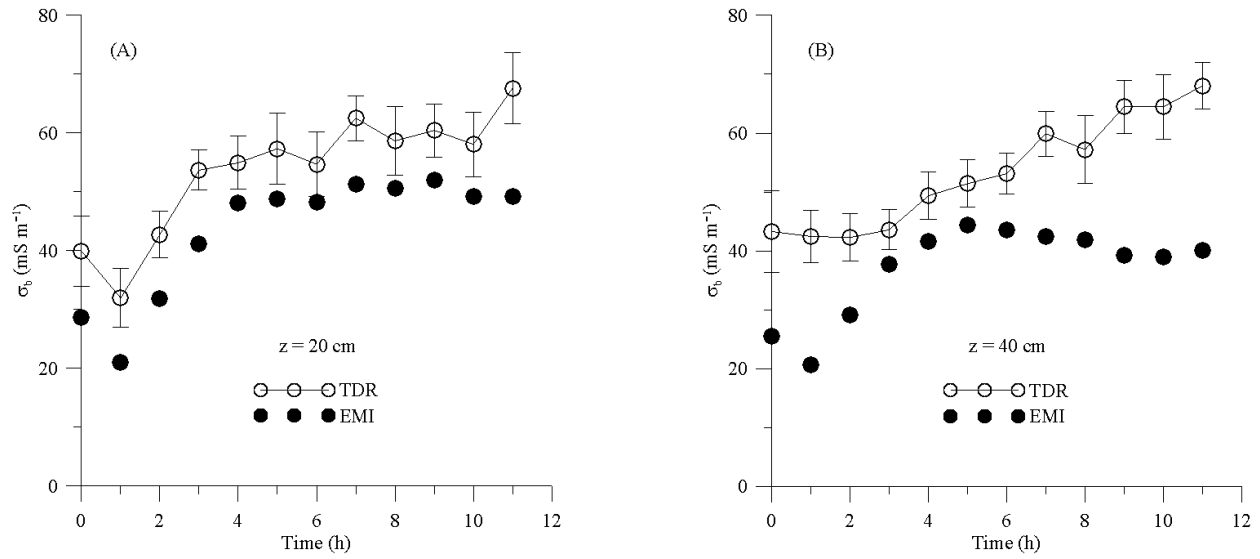
Figure 5 shows the temporal σ_b changes inferred from TDR and EMI observations at two depths, 20 and 40 cm. As reported by some authors (e.g. Coppola et al., 2016; Dragonetti et al., 2018), both techniques provide σ_b estimations but a direct comparison between σ_b by TDR and EMI is not straightforward due to different observation volumes of the two sensors. As argued by Coppola et al. (2016), “because of its relatively small observation volume, a TDR probe provides a quasi-point-like measurements and do not integrate the small-scale variability (in soil water content, solute concentrations, etc.) induced by natural soil heterogeneity. By contrast, EMI data necessarily overrule the small-scale heterogeneities seen by TDR probes as they investigate a much larger volume”. However, this comparison can be used as a means to investigate the consistency of the σ_b trends and to provide an insight into the uncertainty associated with the EMI survey and inversion process in resolving the water infiltration process into the soil profile. Note that the average of TDR measurements in four corners at depths of 20 and 40 cm were considered both in this comparison and in the inversion procedure. The average values and the standard deviation of TDR measurements were presented in Fig. 5.

Focusing on the σ_b series inferred from both TDR observations and EMI inversion, a similar time pattern of σ_b variability is evident, but in general, the EMI model underestimates the σ_b obtained by TDR. A better agreement was observed at 20 cm in terms of both absolute σ_b values and trend ($r=0.94$; Mean Error= 10.1 mS m^{-1}). In contrast, at 40 cm, the mismatch between TDR observations and EMI inversions becomes larger at the end of the experiment. The EMI σ_b values – especially at 40 cm depth – remain rather invariant in the last part of the infiltration experiment. The general outcome that for both layers the EMI σ_b values underestimate the TDR σ_b measurements has been frequently found in the literature (e.g. Coppola et al., 2015; Dragonetti et

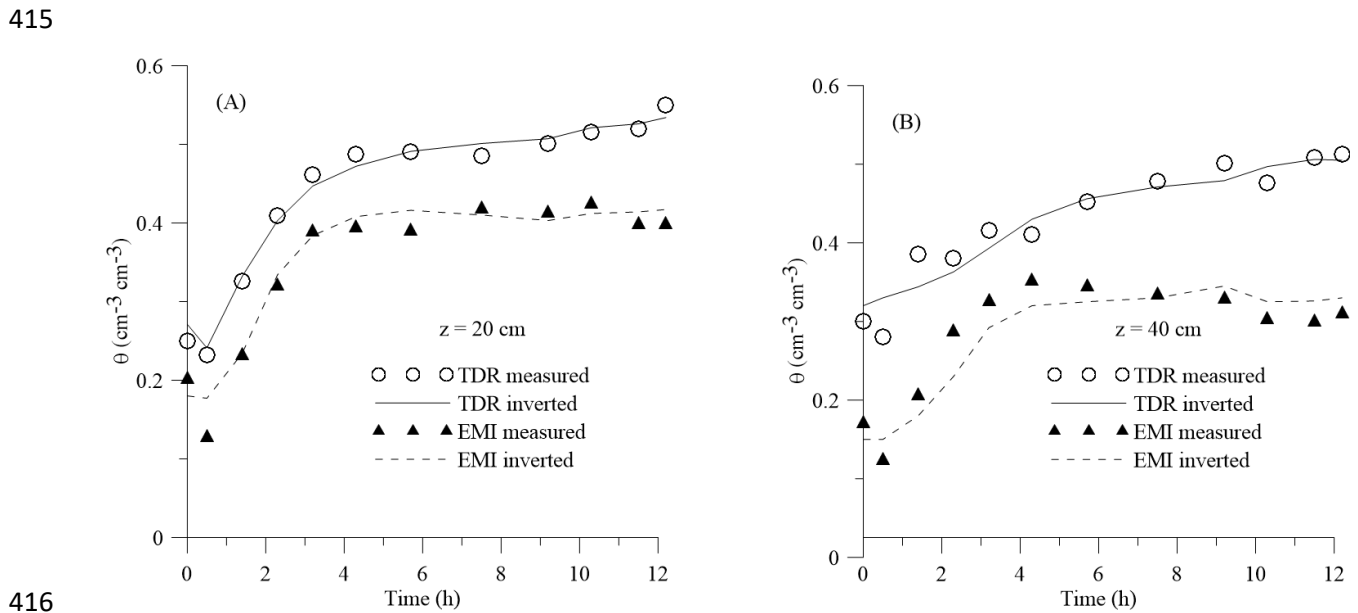
394 al., 2018; Visconti and De Paz, 2021). von Hebel et al. (2014) also found a similar behaviour when
395 comparing their EMI results with ERT surveys. In that case, the σ_a values measured by EMI
396 systematically underestimated the σ_a generated by applying EMI forward modelling to the σ_b
397 distribution retrieved from the ERT surveys. Furthermore, TDR measurements show a low local
398 variability, as depicted in Fig. 5 by the error bars reporting the standard deviation of the σ_b as
399 measured by the four TDR probes.

400 Figure 6 shows the evolution of θ at the same two depths, 20 and 40 cm as observed by
401 TDR and EMI sensors. TDR provides the direct in-situ measurement of θ . In contrast in order to
402 estimate θ from EMI observation, σ_b values extracted at these depths (Fig. 4) were converted to θ
403 by the calibration performed in the laboratory, as detailed in Farzamian et al., (2021). A rapid
404 increase of θ is visible shortly after injection in both EMI-based and TDR-based measurements.
405 The EMI-based θ estimation is able to detect the similar water content evolution (similar water
406 content differences over time) observed by TDR measurements but at a different water content
407 level. Specifically, EMI water contents were lower than the TDR ones but the two series showed
408 a quasi-parallel evolution at 20 cm depth ($r=0.98$; Mean Error= $0.09 \text{ cm}^3 \text{ cm}^{-3}$), while diverging for
409 longer times at 40 cm depth ($r=0.60$; Mean Error= $0.17 \text{ cm}^3 \text{ cm}^{-3}$).

410



411
 412 Figure 5. σ_b evolution estimated from the TDR and EMI measurements at 20 cm (A) and 40 cm
 413 (B) depths. The vertical bars represent the standard deviation of the measurements obtained by the
 414 four TDR sensors.



416
 417 Figure 6. Evolution of θ measured by TDR (circles) and estimated from EMI measurements
 418 (triangles) at 20 cm (A) and 40 cm (B) depths. Continuous lines for TDR and dashed lines for EMI
 419 refer to the estimation obtained by the inversion procedure of the water infiltration process (see
 420 Sect. 4.1.3 below).

421

422 4.1.3. *Estimation of hydraulic properties*

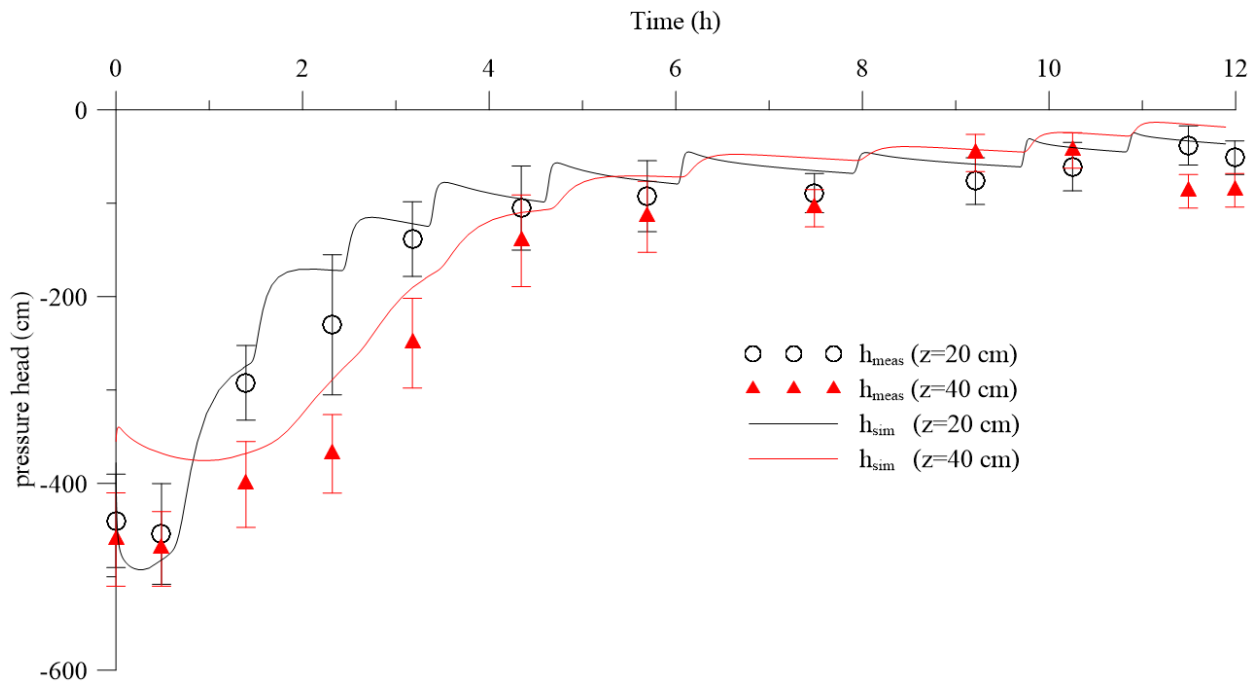
423 In order to estimate hydraulic properties parameters, an inversion procedure was carried
424 out applying HYDRUS-1D. The first set of hydraulic parameters was obtained by using the soil
425 water contents measured by TDR and the pressure heads measured by tensiometers as measured
426 data in the objective function for the optimization procedure (TDR-based). The second set of
427 hydraulic parameters was obtained by using the soil water contents estimated by EMI
428 measurements as measured data (EMI-based). The inversion simulations were carried out by fixing
429 $\theta_r=0$ and $\tau=0.5$, while θ_s , α , n and K_s were optimized for both the Ap and the Bw layers. The
430 hydraulic properties of the bedrock were already known and fixed to $\theta_r=0.068$, $\theta_s=0.354$, $\alpha=0.055$,
431 $n=3.67$, $\tau=0.5$ and $K_s=19.02$ according to Caputo et al. (2010; 2015). We want to stress here that
432 an a-priori characterization of the bedrock layer is not essential and the proposed procedure holds
433 independently on the presence of bedrock. We could have treated the bedrock layer as any other
434 layer in the soil profile, but inserting TDR probes and tensiometers into bedrock presents
435 difficulties. Therefore, we decided to fix the bedrock parameters to the values already available
436 from independent measurements. In different soils with either deeper or absent bedrock, we could
437 have inserted TDR probes into deeper layers of the profile and applied the procedure to any of
438 them.

439 In the inversion procedure, the parameters were determined separately for each horizon of
440 the profile. First, the parameters for the topsoil were estimated and these parameters were then
441 treated as known for the second layer estimation. According to Abbaspour et al. (1999), this
442 approach makes parameter estimation of multi-layered profiles more feasible and accurate. It
443 should be noted that in the case of the TDR-based estimations, optimization involved both

444 measured water contents and pressure head data, whereas the EMI-based estimations only involved
445 “measured” water contents.

446 Figure 6 reports a comparison between water contents measured (symbols) and estimated
447 (lines) by the inversion procedure. The θ evolution was properly estimated at 20 cm depth in both
448 approaches. It is worth noting here that, despite the differences in the absolute value of the water
449 contents, a clear parallel behaviour of the two curves was observed, suggesting similar water
450 content changes over time. A lower agreement was obtained at 40 cm but still reproduced similar
451 water content changes over time. This is a crucial point in this paper, as it is the main reason for
452 the shape of the hydraulic properties we found for the TDR and EMI-based estimations.

453



454

455 Figure 7. Evolution of pressure head at 20 and 40 cm depth measured by tensiometers (symbols)
456 and estimated by the inversion procedure (lines) of the water infiltration process. The vertical bars
457 represent the standard deviation of the measurements obtained by the four tensiometers.

458

459 Similarly, in Fig. 7 the measured (points) and estimated (lines) values of pressure heads
 460 are shown. The simulated values of pressure head well follow the measured one ($r=0.950$ at 20 cm
 461 and $r=0.986$ at 40 cm depth). Furthermore, the error bars, reporting the standard deviation of the
 462 pressure head as measured by the four tensiometers, overlap when the profile is wet (i.e. after the
 463 6th irrigation) and separate during the wetting process.

464 Table 1 reports the parameters of the hydraulic functions, estimated for the first two
 465 horizons and Fig. 8 reports the water retention curves and the hydraulic conductivity curves
 466 corresponding to the parameters shown in table 1 for a better comparison between TDR-based and
 467 EMI-based hydraulic properties assessment. Note in the table the high values of n and K_s for the
 468 bedrock, which indicate a high conductive porous medium. It is possible to explain this by
 469 considering that the bedrock is fractured calcareous, which, contrary to expectation, does not
 470 impede water flow.

471

472 Table 1. vG-M Hydraulic parameters (Eqs. 7 and 8) and dispersivity, λ (Eq. 6) as estimated for Ap
 473 and Bw horizons, and fixed for the bedrock layer.

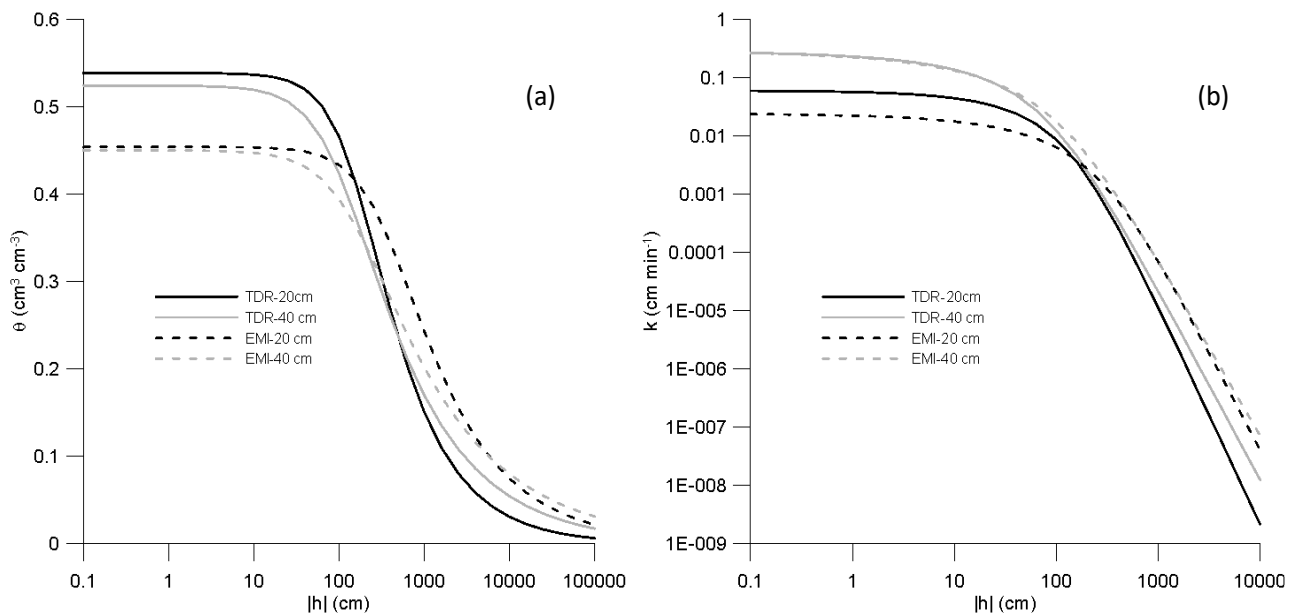
Soil hydraulic and transport parameters*		Ap		Bw		Bedrock
		TDR-based	EMI-based	TDR-based	EMI-based	Fixed a-priori
θ_s	[cm ³ cm ⁻³]	0.54	0.45	0.52	0.45	0.354
α	[cm ⁻¹]	0.006	0.003	0.009	0.007	0.055
n	[-]	1.70	1.54	1.50	1.41	3.67
k_s	[cm min ⁻¹]	0.06	0.02	0.28	0.29	19
λ	[cm]	10	12	0.5	0.8	30

474 * For all horizons $\theta_r=0$ and $\tau=0.5$.

475 As for water retention, the TDR and EMI water retention curves showed similar shapes but
 476 with slightly different saturated water contents. As discussed earlier, the lower saturated water
 477 content is not surprising for the EMI-based estimation due to the overall underestimation of water
 478 content. The two curves almost overlapped once scaling the EMI curve by the ratio of the saturated

479 water contents. Obviously, this result is consistent with the underestimation of EMI-based θ
480 distributions as shown in Fig. 6.

481 As for the hydraulic conductivity, TDR-based and EMI-based hydraulic conductivity
482 curves at both 20 and 40 cm appear to almost overlap, with similar saturated hydraulic conductivity
483 and curve shape. This result is expected because the hydraulic conductivity is mainly a function of
484 the variation of θ and not the absolute value of θ itself. It is worth mentioning that the same top
485 boundary flux and different water contents in the soil profile provided similar EMI-based and
486 TDR-based hydraulic conductivity. These conditions led to two different water flow processes,
487 with simulations predicting higher water stored in the soil profile and lower downward fluxes (data
488 not shown) when TDR-based results are compared to the EMI-based results.



489
490 Figure 8. Soil water retention (A) and unsaturated hydraulic conductivity (B) curves, estimated
491 from the TDR and EMI measurements at 20 cm and 40 cm depths.

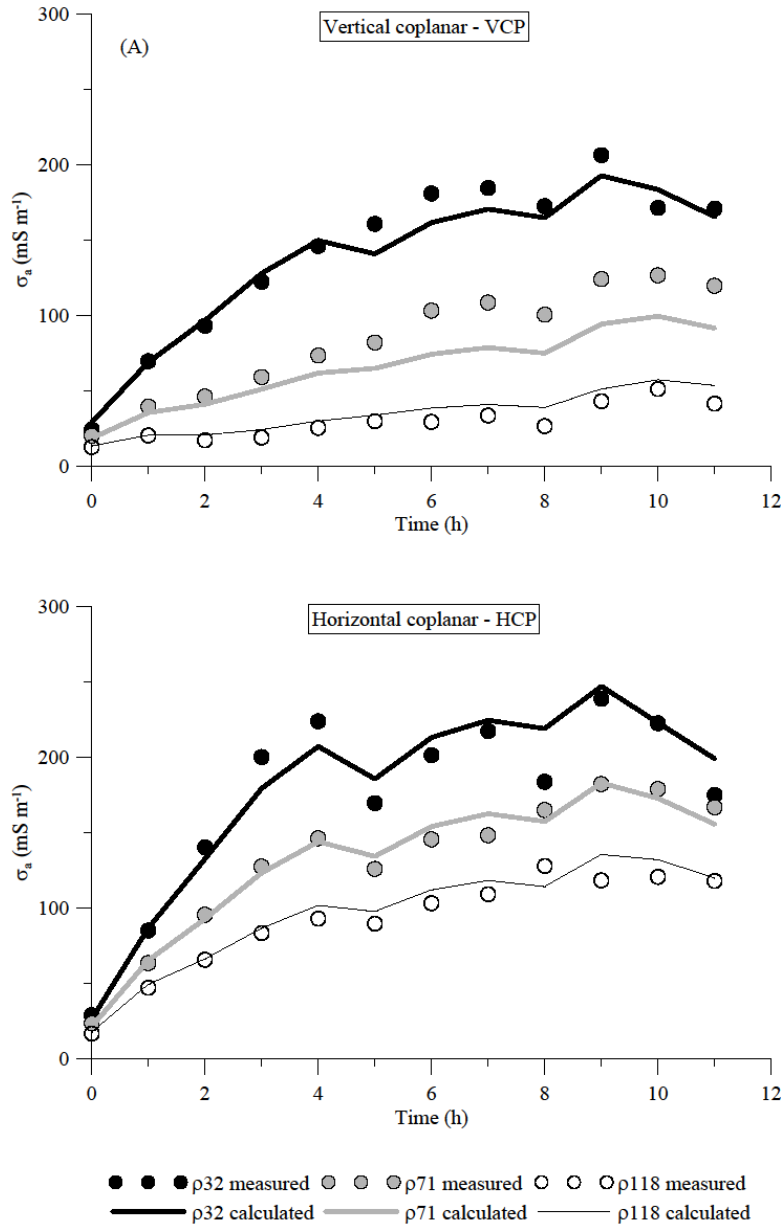
492
493
494

4.2. Solute Infiltration – 2nd Experiment

4.2.1. Time-lapse σ_a data and estimation of σ_b distribution

Figure 9 shows the σ_a data collected during the solute infiltration experiment. Again, as for the 1st experiment, both VCP and HCP modes show a relatively similar pattern of σ_a values with $\rho32$ and $\rho118$ being the highest and lowest respectively. HCP mode shows higher values on average compared to the VCP mode. Similarly, to the water infiltration experiment, σ_a increases consistently during the first three hours of the experiment, then it does not change significantly or consistently until the end of the experiment. Much higher ranges of σ_a variations were measured in both VCP and HCP configurations, with σ_a values ranging in 20-200 and 50-250 mS m⁻¹ respectively.

Figure 10 depicts the σ_b evolution for the 2nd experiment, obtained by time-lapse inversion of σ_a data. σ_a measurements and model response agrees fairly as shown in Fig. 9, however a slight shift can be noticed in the $\rho71$ - VCP mode between data and model response. The results show the rapid evolution of the conductive zone to the soil profile shortly after the irrigation started. In comparison to the obtained σ_b in the 1st experiment, the results reveal significantly higher soil conductivity in topsoil but a much slower evolution. The conductivity of the top layer exceeds 300 mS m⁻¹ shortly after the irrigation. The higher topsoil conductivity results from injection of high-saline water (about 15 dS m⁻¹) that dramatically increases soil conductivity whereas the smaller evolution of the conductive zone is caused by significantly slower concentration propagation into the soil profile.

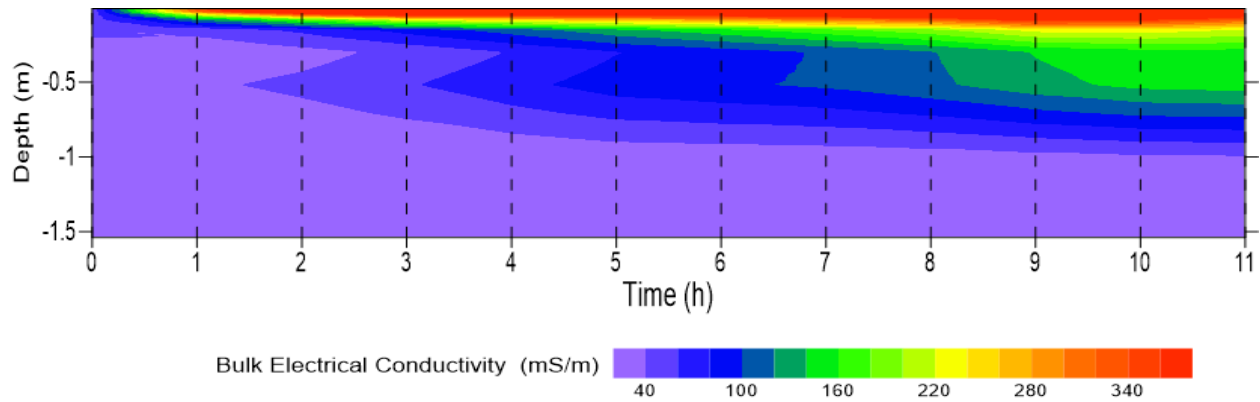


516

517 Figure 9: σ_a values observed during the solute infiltration experiment. (A) VCP, (B) HCP. The
 518 symbols represent the measured data whereas the lines represent the values calculated after the
 519 inversion.

520

521



522

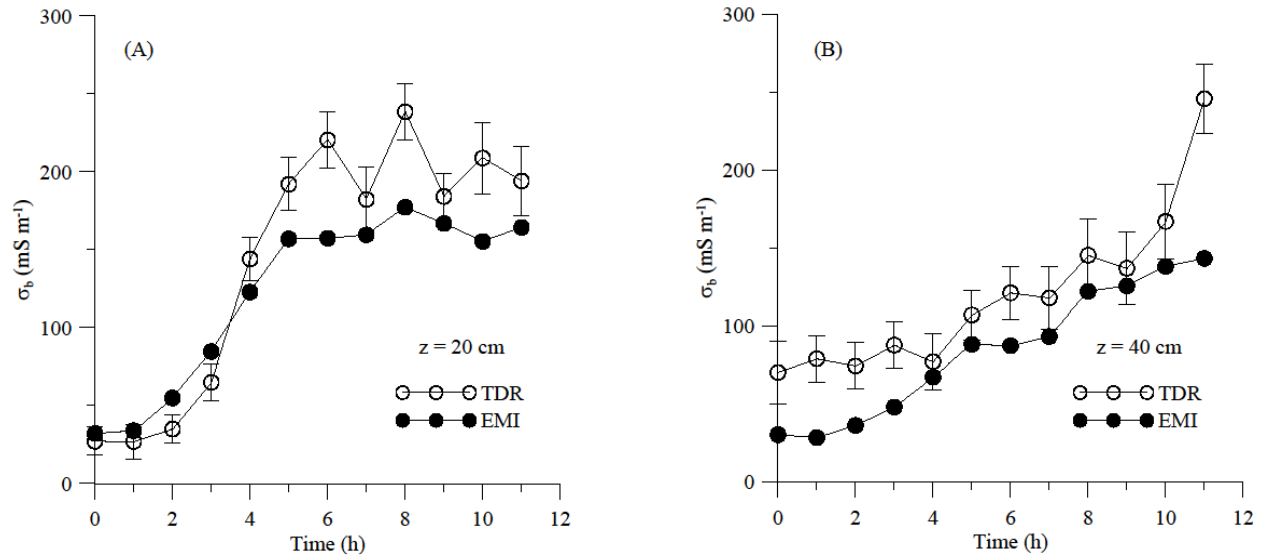
523 Figure 10. Time evolution of bulk electrical conductivity (σ_b) during the solute infiltration
 524 experiment.

525

526 4.2.2. Comparison between TDR-based and EMI-based σ_b and $[Cl^-]$ distributions

527

528 Figure 11 shows the comparison between the σ_b values obtained by the TDR measurements
 529 and those obtained from the EMI inversion (Fig. 10) during the 2nd experiment. As discussed
 530 above, this comparison is to provide an insight into the potential of the EMI survey and inversion
 531 process in monitoring a solute transport experiment into a soil profile. The comparison shows a
 532 similar time pattern of σ_b variability, but in general the EMI model underestimates the σ_b obtained
 533 by TDR. The results of this comparison agree with the 1st experiment where, again, the EMI-based
 534 σ_b are lower compared to those measured by the TDR. In contrast to the 1st experiment, the
 535 differences between the two techniques and in terms of the absolute σ_b values are of minor concern.
 536 This could be due to the larger conductivity contrast that tracer introduced into the soil profile in
 537 the 2nd experiment which became easier to detect by using the EMI sensor. On the other hand, the
 538 TDR probes show more fluctuations in σ_b measurements, especially at 20 cm. We attribute these
 539 fluctuations to the smaller volume of investigation of the TDR probes which are very sensitive to
 540 the process taking place very close to the probe and, therefore, strongly influenced by small-scale
 heterogeneities.



541
 542 Figure 11. σ_b evolution estimated by TDR and EMI measurements at 20 cm (A) and 40 cm (B)
 543 depth.

544
 545 The next step in the procedure allows us to determine the distribution of Cl^- concentrations
 546 by EMI sensors (Sect. 4.2.3.) used for estimating the longitudinal dispersivity of the two soil layers
 547 investigated. For the sake of comparison, TDR-based $[\text{Cl}^-]$ distributions were obtained directly in
 548 the field from a direct measurement of the impedance Z along the TDR transmission line embedded
 549 in the soil. As for the EMI-based Cl^- concentrations, a forward HYDRUS-1D simulation was
 550 carried out using the EMI-based hydraulic properties obtained from the 1st experiment and reported
 551 in Table 1 to estimate the water content distributions in correspondence with the EMI measurement
 552 times of the 2nd experiment. These water contents, combined with the available σ_b distribution
 553 obtained from the EMI inversion, allowed us to obtain the σ_w distributions (through the θ - σ_b - σ_w
 554 calibration relationship) for both depths and, consequently, the $[\text{Cl}^-]$ distributions.

555

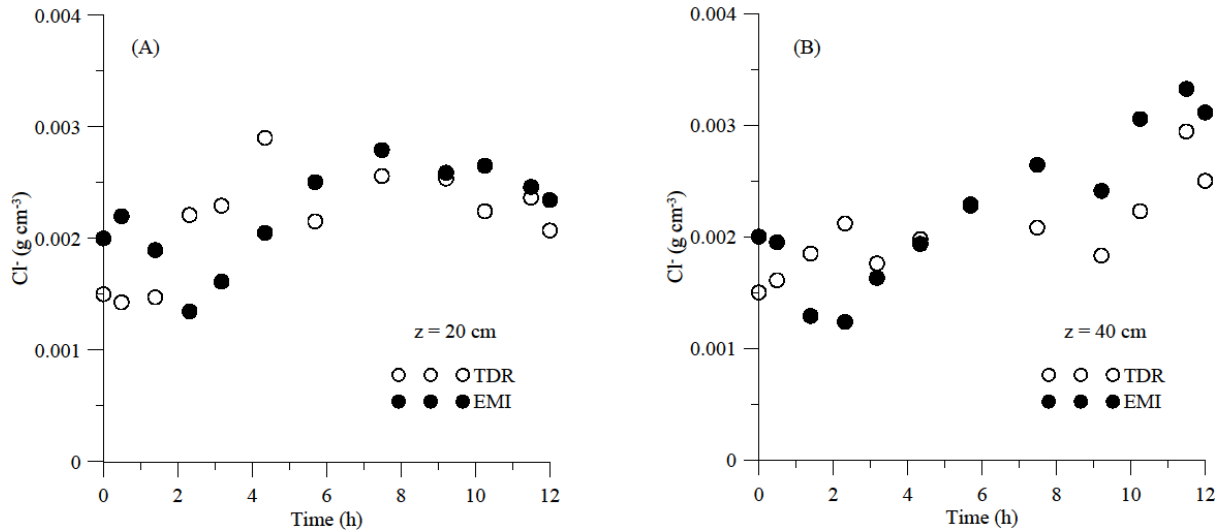


Figure 12. $[\text{Cl}^-]$ distributions inferred from EMI and TDR measurements, at 20 (A) and 40 (B) cm depth.

556 Figure 12 shows the $[\text{Cl}^-]$ distributions inferred from EMI compared to the TDR
 557 measurements. The comparison suggests a good agreement between the two time-series. The EMI-
 558 based concentrations underestimate – on average – the TDR-based ones by 4% and by 7% at 20
 559 cm and 40 cm depths, respectively. The time evolution of the two data series reveals marked
 560 differences, as shown by the very different correlation: $r = -0.04$ for the 20 cm depth and $r = 0.70$
 561 for the 40 cm depth. The difference between the two data series at both depths can be mostly
 562 explained by the differences between σ_b distributions shown in Fig. 11. Additionally, another point
 563 of difference may arise from the assumption that the water content distribution obtained from the
 564 HYDRUS-1D simulation can be used as a substitute for the water content measurements, in order
 565 to obtain $[\text{Cl}^-]$ from the EMI readings.

4.2.3. Estimation of longitudinal dispersivity

567 Inverse HYDRUS-1D simulations were conducted using concentration data provided by both
 568 the TDR and EMI results, in order to estimate the longitudinal dispersivity for both Ap and Bw
 569 horizons. The results are reported in the last row of Table 1. TDR-based and EMI-based procedures

570 provide similar values of λ . Specifically, for the Ap horizon, the obtained values agree with those
571 frequently found in the literature for either large columns or field-measured dispersivity (e.g.
572 Vanderborght and Vereecken, 2007; Coppola et al., 2011). The TDR and EMI-based estimation
573 of dispersivity for the Bw horizon shows one order of magnitude lower values compared to the Ap
574 horizon. These values are more consistent with values measured in the laboratory (Coppola et al.,
575 2019). For column scale (undisturbed soil monoliths with a length > 30 cm), Vanderborght and
576 Vereecken (2007) found values in the order of 10 cm. The same values were found by Coppola et
577 al. (2011) at both plot and transect scales. Note in the Table 1 the high value of dispersivity used
578 for the bedrock layer. This is consistent with the nature of the bedrock, which, as mentioned, is a
579 fractured calcareous and highly conductive rock, which may well explain high dispersivity values.

580

581 **5. FURTHER DISCUSSION ON THREE KEY POINTS OF THE PROPOSED**
582 **APPROACH**

583 Following, our discussion will focus on three major aspects of this research in terms of the
584 choice of approach (uncoupled vs coupled), the suitability of EMI as a replacement for invasive
585 sensors, and EMI-related sources of uncertainty.

586 **5.1. Uncoupled vs Coupled approach**

587 In hydro-geophysical studies there is an ample debate on this issue. Camporese et al., 2014,
588 stated in their conclusions: “the relative merit of the coupled approach versus the uncoupled one
589 cannot be assumed a priori and should be assessed case by case. As the information content of the
590 geophysical data remains the same in both the coupled and uncoupled methods, the main difference
591 is the approach taken in order to complement the information content and construct an “image”

592 of the process”. Based on the methodology proposed in this paper and the corresponding results,
593 the following discussion aims to better clarify why we applied an uncoupled approach.

594 Let’s refer to the vertical water infiltration process monitored by the EMI sensor during the 1st
595 experiment and producing direct measurements of apparent electrical conductivity (σ_{a_meas}). In a
596 coupled approach, the hydrological model is the starting point of the procedure. Guess values of
597 hydraulic and dispersive parameters are initially fixed; thus, a hydrological simulation is carried
598 out producing water content distributions along the soil profile, evolving over time. These water
599 content distributions are converted to corresponding distributions of bulk electrical conductivity,
600 σ_b , by using an empirical relationship (e.g. Binley et al., 2002). These σ_b distributions, in turn, are
601 used as input in an EM forward modelling to produce the estimations of apparent electrical
602 conductivity (σ_{a_est}). In this approach, the objective function involves the residuals ($\sigma_{a_meas} - \sigma_{a_est}$).
603 This objective function is eventually minimised by optimising the hydraulic parameters in the
604 hydrological model.

605 The main strength of this approach relies on the fact that no EMI inversion is required. Also,
606 as discussed by Hinnell et al. (2010), the attractiveness of the coupled approach is that the
607 hydrologic model may provide the physical context for a plausible interpretation of the geophysical
608 measurements. Yet, this strength is counterbalanced by a weakness which is crucial in view of
609 simplifying the experimental requirements of hydraulic characterization. Actually, an instrumental
610 shift in EMI σ_a readings has been frequently observed when compared to other sources of
611 measurements such as ERT data (von Hebel et al., 2014; 2019) or direct measurements of TDR
612 (Dragonetti et al. 2018). In the context of a hydraulic parameter estimation procedure, this is a
613 crucial point, as it means that EMI measurements do not immediately provide correct electrical
614 conductivity distributions. Thus, the coupled approach always requires an independent dataset,

615 obtained by different sensors (e.g. ERT, TDR, sampling) to remove the shift in the EMI σ_a
616 readings. Such a scheme would be contrary to the spirit of our paper, which mainly aims at
617 minimising the sensors and the data necessary for in-situ soil hydraulic characterization.

618 In an uncoupled approach, the geophysical model is the starting point of the procedure. As a
619 result of geophysical inversion, the σ_b distributions are derived, which are then converted to as
620 many distributions of water content (θ_{meas}) through an empirical relationship, determined from
621 laboratory analysis. Afterward, the hydrological model estimates water contents (θ_{est}), and the
622 objective function, involving the residuals ($\theta_{\text{meas}} - \theta_{\text{est}}$), is eventually minimised by optimising the
623 hydraulic parameters. The main weakness of this approach corresponds to the strength of the
624 coupled approach. The uncoupled approach requires geophysical inversion, involving the
625 uncertainty source coming from the ill-posedness problem. However, the main strength of the
626 methodology we propose in our paper – a fast in-situ non-invasive method to estimate soil
627 hydraulic and transport properties at plot scale – does not require preliminary removal of the
628 (unknown) shift in the EMI readings by additional field measurements with other sensors.
629 Conversely, the shift effect is implicitly kept in the σ_b distributions, from this in the measured
630 water content distributions and finally included in the hydrological inversion. This allowed us to
631 reveal the effects of technical limitations of the EMI sensor including the instrumental shift in EMI
632 σ_a readings in the water content estimations and from this in the hydraulic properties' estimation.
633 In the 1st experiment, by comparing the EMI-based water contents to the water contents coming
634 from TDR, it was possible to see that the shift in the EMI readings produced quasi-parallel water
635 content evolutions, thus meaning that the EMI shift is rather stable with water content change.
636 Related to this, in terms of hydraulic properties, the shift simply results in scaled saturated water
637 content. This may well be explained physically by just considering the parallel behaviour of the

638 water contents over time signifies similar water content changes over time. This is translated in
639 similar hydraulic conductivities, which in the van Genuchten-Mualem model means similar α and
640 n parameters, and thus water retention curves are simply scaled by the saturated water content
641 ratio.

642 As an additional benefit of an uncoupled approach, it allows for the sequential estimation of
643 parameters (from the upper to the lower horizon), which can reduce the problems of parameter
644 correlation and uniqueness. In this work, the parameters were estimated separately for each horizon
645 of the profile according to Abbaspour et al. (1999). This approach makes parameter estimation of
646 multi-layered profiles more feasible and accurate, however, this cannot be done within a coupled
647 model. If more than one layer has to be characterised, the coupled approach requires that all the
648 parameters have to be simultaneously optimised. This is because the electrical conductivity
649 distribution of the whole soil profile must be first simulated in order to generate required σ_{a_est} to
650 compare to σ_{a_meas} in the objective function.

651

652 **5.2. Suitability of EMI as a replacement for invasive sensors**

653 The proposed methodology for the estimation of vG-M parameters proved to be effective for
654 both Ap and Bw horizons. The overall EMI-based underestimation of θ did not impact the
655 hydraulic conductivity curves significantly as the hydraulic conductivity is mainly function of the
656 variation of θ and not of its absolute value. On the other hand, this underestimation resulted in
657 lower saturated water content which also appeared in the water retention curve. The latter can be
658 simply converted to more accurate water content distribution by direct measurement of the actual
659 saturated water content at the end of the experiment using TDR probes or even by taking soil
660 samples for laboratory weight.

661 In terms of the longitudinal dispersivity, λ , there was a very good agreement between EMI-
662 based and TDR-based estimation for both Ap and Bw horizons. The finding results are also in very
663 good agreement with previous in-situ and laboratory measurements. However, this method
664 requires that the hydraulic properties of the investigated soil at the scale of concern be assessed
665 prior to the application of this method to discriminate the contribution of water content and
666 concentration in the EMI-based σ_b estimation.

667

668 **5.3. EMI-related sources of uncertainty**

669 The application of EMI for detailed investigation of the infiltration process has several
670 limitations, apart from the potential instrumental drift of EMI sensor and the overall
671 underestimation of water content and concentration, and requires further investigation. Resolving
672 the wetting zone during the water injection is one source of uncertainty in this approach. The water
673 content sharply decreases with depth in this zone to near the initial water content of the soil and
674 causes dramatic resistivity variation. The limited number of σ_a measurements (total of 6) is not
675 sufficient for recovering the sharp σ_b variability that takes place during the infiltration. In addition,
676 a smoothness constraint was performed in the inversion process to stabilize the inversion process
677 which further smooths the layer boundaries in this approach. Resolving the shallow bedrock
678 interface at depth and beneath a conductive zone was also very challenging. This is because the
679 sensitivity of the EMI signals is generally very limited over the resistive zone and the condition
680 becomes much worse when the resistive zone (bedrock) is located beneath a conductive zone
681 (tracer): the EMI response of the subsurface is dominated by the influence of the near-surface
682 conductive zone. In addition, five of the six depths of investigation of the CMD Mini-Explorer are
683 limited to the first 1 m, and, as a result, a lower resolution is expected at greater depths. This
684 resulted in an even larger underestimation of soil conductivity on top of the bedrock and an

685 overestimation of bedrock conductivity in the close vicinity of soil. These findings from synthetic
686 studies and modelling field data are similar to those reported in Farzamian et al. (2021) due to the
687 similarity of the site, experiment, and the use of the same EMI sensor. Measuring σ_a at different
688 heights or using different EMI sensor with larger number of receivers such as CMD Mini-Explorer
689 6L enables us to collect more σ_a data to better resolve changes that occur over short depth
690 increments. To this aim, the EMI configuration and data survey can also be optimized using
691 optimization techniques such as machine learning based methods, given the specific survey goals
692 and independent knowledge of the subsurface electrical properties, as shown for example by van't
693 Veen et al. (2022).

694

695 **6. CONCLUSION**

696 In this paper, we proposed a non-invasive in-situ method integrating EMI and hydrological
697 modelling to estimate soil hydraulic and transport properties at the plot scale. For this purpose, we
698 carried out two experiments involving 1) water infiltration and 2) solute transport over a 4 x 4 m
699 plot. The propagation of wetting front and solute concentration along the soil profile in the plot
700 was monitored using an EMI sensor (i.e. CMD mini-Explorer) and for the sake of procedure
701 evaluation Time Domain Reflectometry probes and tensiometers. Time-lapse apparent electrical
702 conductivity (σ_a) data obtained from the EMI sensor were inverted to estimate the evolution over
703 time of the vertical distribution of the bulk electrical conductivity (σ_b). The σ_b distributions were
704 converted to water content and solute concentration by using a standard laboratory calibration,
705 relating σ_b to water content (θ) and soil solution electrical conductivity (σ_w).

706 Based on the first water infiltration experiment, the soil water retention and hydraulic
707 conductivity curves were then obtained for two layers of the soil profile by an optimization

708 procedure minimizing the deviations between the numerical solution of the water infiltration
709 experiment and the estimated water contents inferred from the EMI results. EMI-based hydraulic
710 properties were very similar in shape to those obtained by TDR and tensiometers data. This shape-
711 similarity allowed to convert the EMI-based hydraulic properties to the TDR-based ones by simply
712 scaling them by the ratio of the saturated water content for both the soil layers considered. This
713 was a crucial finding in this paper and was mainly ascribed to the fact that the water content
714 changes over time detected by the EMI closely followed those observed by TDR. These EMI-
715 based hydraulic properties were then used as input for hydrological modelling of the second solute
716 transport experiment. This allowed discriminating water content and solute concentration
717 components in the EMI σ_b distributions obtained during the second experiment. These
718 concentrations were afterward used to estimate the dispersivity based on an inversion procedure
719 minimizing the residuals of EMI-based concentration and those simulated by the hydrological
720 model. The reliability of the EMI-based hydraulic properties allowed us to obtain estimations of
721 the dispersivity comparable to those obtained by the same optimization procedure applied to the
722 TDR data.

723 The overall results show the high potential of the EMI sensor to replace TDR and tensiometer
724 probes in the assessment of soil hydraulic properties. In practice, one could monitor a relatively
725 short infiltration experiment with an EMI sensor and use the water content estimations in an
726 inversion procedure to estimate the hydraulic properties. The underestimated water content
727 observed in the first experiment can be converted to more accurate water content distribution by
728 direct measurement of the actual saturated water content at the end of the experiment using TDR
729 probes or even by taking samples and laboratory measurements.

730 The EMI-based estimation of longitudinal dispersivity, λ agrees well with TDR-based
731 estimation as well as previous in-situ and laboratory measurements which suggests that the
732 proposed methodology can be used in the assessment of this parameter which is indeed an
733 important parameter in soil salinity simulations in salt-affected regions across the world. However,
734 estimating λ based on only a solute infiltration test is not feasible as the temporal variability of σ_b
735 is a function of both water content and concentration changes. We proposed the sequence of water
736 and solute infiltration tests to discriminate the contribution of the water content and the soil
737 solution electrical conductivity to the EMI-based σ_b .

738 Water irrigation and soil salinity management and thus hydrological investigations are usually
739 field and even large-scale challenges. The EM method is a non-invasive, fast, and cost-effective
740 technique, covering large areas in less time and at a lower cost. Although our study was limited to
741 a controlled experiment on a plot scale and a single study report, scaling up from plot scale to field
742 scale assessment might be feasible due to the method's potential for rapid data collection. More
743 investigations have to be conducted in this area to evaluate the potential of EMI sensors under
744 different soil conditions and within the larger 2D and 3D investigations to further address the
745 limitations of this methodology at different scales.

746

747 **ACKNOWLEDGMENTS**

748 This work was funded in the scope of the project SALTFREE: Salinization in irrigated areas: risk
749 evaluation and prevention [ARIMNet2, Grant agreement no. 618127], by the Italian Ministry of
750 Agricultural, Food and Forestry Policies [D.M. 28675/7303/15]. M. Farzamian was supported by

751 a contract within project SOIL4EVER [Increasing water productivity through the sustainable use
752 of soils, PTDC/ASP-SOL/28796/2017].

753

754 **REFERENCES**

755 Abbasi, F., Šimůnek, J., Feyen, J., van Genuchten, M.T., and Shouse, P.T.: Simultaneous inverse
756 estimation of soil hydraulic and solute transport parameters from transient field experiments:
757 Homogeneous soil. *Transactions of the ASAE* 46(4): 1085, 2003.

758 Archie, G.E.: The electrical resistivity log as an aid in determining some reservoir characteristics.
759 *Transactions of the AIME* 146(01): 54–62, 1942.

760 Basile, A., Coppola, A., De Mascellis, R., and Randazzo, L.: Scaling Approach to Deduce Field
761 Unsaturated Hydraulic Properties and Behavior from Laboratory Measurements on Small
762 Cores, *Vadose Zone J.*, 5, 1005–1016, <https://doi.org/10.2136/vzj2005.0128>, 2006.

763 Binley, A., Cassiani, G., Middleton, R., and Winship, P.: Vadose zone flow model
764 parameterisation using cross-borehole radar and resistivity imaging. *Journal of Hydrology*
765 267(3–4): 147–159, [https://doi.org/10.1016/S0022-1694\(02\)00146-4](https://doi.org/10.1016/S0022-1694(02)00146-4), 2002.

766 Bouksila, F., Persson, M., Bahri, A., and Berndtsson, A.: Electromagnetic induction prediction of
767 soil salinity and groundwater properties in a Tunisian Saharan oasis. *Hydrological sciences*
768 *journal* 57(7): 1473–1486, <https://doi.org/10.1080/02626667.2012.717701>. 2012.

769 Camporese, M., Cassiani G., Deiana R., Salandin P., and Binley A.: Coupled and uncoupled
770 hydrogeophysical inversions using ensemble Kalman filter assimilation of ERT-monitored
771 tracer test data, *Water Resour. Res.*, 51, 3277–3291, doi:10.1002/2014WR016017. 2015

772 Caputo, M.C., De Carlo, L., Masciopinto, C., and Nimmo, J.R.: Measurement of field-saturated
773 hydraulic conductivity on fractured rock outcrops near Altamura (Southern Italy) with an
774 adjustable large ring infiltrometer, *Environ. Earth Sci.*, 60, 583–590,
775 <https://doi.org/10.1007/s12665-009-0198-y>, 2010.

776 Caputo M.C., Maggi S., and Turturro A.C.: Calculation of Water Retention Curves of Rock
777 Samples by Differential Evolution, in: *Engineering Geology for Society and Territory*, edited
778 by Lollino G., Manconi A., Guzzetti F., Culshaw M., Bobrowsky P., Luino F. (eds), Volume 5,
779 Springer, Cham, <https://doi.org/10.1007/978-3-319-09048-1>, 2015.

780 Coppola, A., Comegna, A., Dragonetti, G., Dyck, M., Basile, A., Lamaddalena, N., Kassab, M.,
781 and Comegna, V.: Solute transport scales in an unsaturated stony soil, *Adv. Water Resour.*, 34,
782 747–759, <https://doi.org/10.1016/j.advwatres.2011.03.006>, 2011.

783 Coppola, A., Smettem, K., Ajeel, A., Saeed, A., Dragonetti, G., Comegna, A., Lamaddalena, N.,
784 and Vacca, A.: Calibration of an electromagnetic induction sensor with time-domain
785 reflectometry data to monitor rootzone electrical conductivity under saline water irrigation, *Eur.*
786 *J. Soil Sci.*, 67, 737–748, <https://doi.org/10.1111/ejss.12390>, 2016.

- 787 Coppola, A., Dragonetti, G., Comegna, A., Lamaddalena, N., Caushi, B., Haikal, M. A., and
788 Basile, A.: Measuring and modeling water content in stony soils, *Soil Till. Res.*, 128, 9–22,
789 <https://doi.org/10.1016/j.still.2012.10.006>, 2013.
- 790 Coppola, A., Dragonetti, G., Sengouga, A., Lamaddalena, N., Comegna, A., Basile, A., Noviello,
791 N., and Nardella, L.: Identifying Optimal Irrigation Water Needs at District Scale by Using a
792 Physically Based Agro-Hydrological Model. *Water* 11(4). <https://doi.org/10.3390/w11040841>,
793 2019.
- 794 Coppola, A., Chaali, N., Dragonetti, G., Lamaddalena, N., and Comegna, A.: Root uptake under
795 non-uniform root-zone salinity, *Ecohydrology*, 8, 1363–1379,
796 <https://doi.org/10.1002/eco.1594>, 2015.
- 797 Corwin, D. L., and Lesch, S. M.: Apparent soil electrical conductivity measurements in agriculture,
798 *Comput. Electron. Agr.*, 46, 11–43, <https://doi.org/10.1016/j.compag.2004.10.005>, 2005.
- 799 Dane, J. H., & Topp, C. G. (Eds.). (2020). *Methods of soil analysis, Part 4: Physical methods (Vol.*
800 *20)*. John Wiley & Sons.
- 801 Dragonetti, G., Comegna, A., Ajeel, A., Deidda, G. P., Lamaddalena, N., Rodriguez, G., Vignoli,
802 G., and Coppola, A.: Calibrating electromagnetic induction conductivities with time-domain
803 reflectometry measurements, *Hydrol. Earth Syst. Sci.*, 22, 1509–1523,
804 <https://doi.org/10.5194/hess-22-1509-2018>, 2018.
- 805 Ellsworth, T.R., Shaouse, P.J., Jobes, J.A., Fargerlund, J., and Skaggs, T.H.: Solute transport in
806 unsaturated soil: Experimental design, parameter estimation, and model discrimination. *Soil*
807 *Science Society of America Journal* 60(2): 397–407,
808 <https://doi.org/10.2136/sssaj1996.03615995006000020010x>, 1996.
- 809 Farzamian, M., Paz, M. C., Paz, A. M., Castanheira, N. L., Gonçalves, M. C., Monteiro Santos, F.
810 A., and Triantafilis, J.: Mapping soil salinity using electromagnetic conductivity imaging—A
811 comparison of regional and location-specific calibrations, *Land. Degrad. Dev.*, 30, 1393–1406,
812 <https://doi.org/10.1002/ldr.3317>, 2019a.
- 813 Farzamian, M., Ribeiro, J.A., Monteiro Santos, F.A., Khalil M.A.: Application of Transient
814 Electromagnetic and Audio-Magnetotelluric Methods for Imaging the Monte Real Aquifer in
815 Portugal. *Pure Appl. Geophys*, <https://doi.org/10.1007/s00024-018-2030-7>, 2019b.
- 816 Farzamian, M., Autovino, D., Basile, A., De Mascellis, R., Dragonetti, G., Monteiro Santos, F.,
817 Binley, A., and Coppola, A.: Assessing the dynamics of soil salinity with time-lapse inversion
818 of electromagnetic data guided by hydrological modelling, *Hydrol. Earth Syst. Sci.*, 25, 1509–
819 1527, <https://doi.org/10.5194/hess-25-1509-2021>, 2021.
- 820 Groh, J., Stumpp, C., Lücke, A., Pütz, T., Vanderborght, J., Vereecken, H.: Inverse estimation of
821 soil hydraulic and transport parameters of layered soils from water stable isotope and lysimeter
822 data. *Vadose Zone Journal* 17(1): 1–19, <https://doi.org/10.2136/vzj2017.09.0168>, 2018.
- 823 Gómez Flores, J.L., Ramos Rodríguez, M., González Jiménez, A., Farzamian, M., Herencia Galán,
824 J.F., Salvatierra Bellido, B., Cermeño Sacristan, P., Vanderlinden, K.: Depth-Specific Soil
825 Electrical Conductivity and NDVI Elucidate Salinity Effects on Crop Development in
826 Reclaimed Marsh Soils. *Remote Sens.*, 14, 3389. <https://doi.org/10.3390/rs14143389>, 2022.
- 827 Hansen, S., Abrahamsen, P., Petersen, C.T., Styczen, M., 2012. Daisy: model use, calibration and

828 validation. *Trans. ASABE* 55, 1315–1333.

829 Hassan, S.B.M., Dragonetti, G., Comegna, A., Sengouga, A., Lamaddalena, N., Coppola, A., 2022.
830 A Bimodal Extension of the ARYA&PARIS Approach for Predicting Hydraulic Properties of
831 Structured Soils, *Journal of Hydrology* (2022), doi:
832 <https://doi.org/10.1016/j.jhydrol.2022.127980>

833 Hinnell, A.C., Ferre, T.P.A., Vrugt, J.A., Huisman, J.A., Moysey, S., Rings, J., and Kowalsky,
834 M.B.: Improved extraction of hydrologic information from geophysical data through coupled
835 hydrogeophysical inversion. *J. Water Resour. Res.* 46, W00D40,
836 <https://doi.org/10.1029/2008WR007060>, 2010.

837 Huang, J., Monteiro Santos, F. A., and Triantafilis, J.: Mapping soil water dynamics and a moving
838 wetting front by spatiotemporal inversion of electromagnetic induction data, *Water Resour.*
839 *Res.*, 52, 9131–9145, <https://doi.org/10.1002/2016WR019330>, 2016.

840 Inoue, M., Šimuunek, J., Shiozawa, S., and Hopmans, J.W.: Simultaneous estimation of soil
841 hydraulic and solute transport parameters from transient infiltration experiments. *Advances in*
842 *Water Resources* 23(7): 677–688, [https://doi.org/10.1016/S0309-1708\(00\)00011-7](https://doi.org/10.1016/S0309-1708(00)00011-7), 2000.

843 Kaufman, A.A., and Keller, G.V.: *Frequency and Transient Sounding Methods Geochemistry and*
844 *Geophysics*. Elsevier Science Ltd, New york, 1983.

845 Kemna, A., Vanderborght, J., Kulesa, B., and Vereecken, H.: Imaging and characterization of
846 subsurface solute transport using electrical resistivity tomography (ERT) and equivalent
847 transport models. *Journal of hydrology* 267(3–4): 125–146, [https://doi.org/10.1016/S0022-](https://doi.org/10.1016/S0022-1694(02)00145-2)
848 [1694\(02\)00145-2](https://doi.org/10.1016/S0022-1694(02)00145-2), 2002.

849 Koganti, T., Narjary, B., Zare, E., Pathan, A.L., Huang, J., and Triantafilis, J.: Quantitative
850 mapping of soil salinity using the DUALEM-21S instrument and EM inversion software, *Land*
851 *Degradation and Development*, vol. 29, pp. 1768 - 1781, <http://dx.doi.org/10.1002/ldr.2973>,
852 2018.

853 Kroes, J.G., van Dam, J.C., Bartholomeus, R.P., Groenendijk, P., Heinen, M., Hendriks, R. F.A.,
854 Mulder, H.M., Supit, I., van Walsum, P.E.V., 2017. SWAP version 4; Theory_description and
855 user manual. Wageningen, Wageningen Environmental Research, Report 2780. 244 pp.

856 Malicki, M. A. and Walczak, R. T.: Evaluating soil salinity status from bulk electrical conductivity
857 and permittivity, *Eur. J. Soil Sci.*, 50, 505–514, [https://doi.org/10.1046/j.1365-](https://doi.org/10.1046/j.1365-2389.1999.00245.x)
858 [2389.1999.00245.x](https://doi.org/10.1046/j.1365-2389.1999.00245.x), 1999.

859 McLachlan, P., Blanchy, G., and Binley, A.: EMagPy: Open-source standalone software for
860 processing, forward modeling and inversion of electromagnetic induction data. *Computers &*
861 *Geosciences*. <https://doi.org/10.1016/j.cageo.2020.104561>, 2020.

862 Moghadas, D.: Probabilistic Inversion of Multiconfiguration Electromagnetic Induction Data
863 Using Dimensionality Reduction Technique: A Numerical Study, *Vadose Zone J.*, 18, 1–16,
864 <https://doi.org/10.2136/vzj2018.09.0183>, 2019.

865 Monteiro Santos, F. A.: 1D laterally constrained inversion of EM34 profiling data, *J. Appl.*
866 *Geophys.*, 56, 123–134, <https://doi.org/10.1016/j.jappgeo.2004.04.005>, 2004.

867 Paz, M. C., Farzamian, M., Paz, A. M., Castanheira, N. L., Gonçalves, M. C., and Monteiro Santos,
868 F.: Assessing soil salinity using time-lapse electromagnetic conductivity imaging, *SOIL*, 6,

869 499–511, <https://doi.org/10.5194/soil-6-499-2020>, 2020b.

870 Robinson, D.A., Jones, S.B., Wraith, J.M., Or, D., and Friedman, S.P.: A Review of Advances in
871 Dielectric and Electrical Conductivity Measurement in Soils Using Time Domain
872 Reflectometry. *Vadose Zone Journal* 2: 444–475. doi: 10.2136/vzj2003.4440, 2003.

873 Saeed A., Comegna, A., Dragonetti, G., Lamaddalena, N., Coppola, A.: Soil surface electrical
874 conductivity estimated by TDR and EMI sensors: Accounting for the different sensor
875 observation volumes, *J. of Agricultural Engineering*. Vol XLVIII, doi:10.4081/jae.2017.716,
876 2017.

877 Sasaki, Y.: Full 3-D inversion of electromagnetic data on PC. *Journal of Applied Geophysics*
878 46(1): 45–54. doi: 10.1016/S0926-9851(00)00038-0, 2001.

879 Severino G, Comegna A., Coppola A., Sommella A., Santini A.: Stochastic analysis of a field-
880 scale unsaturated transport experiment, *Advances in Water Resources*,
881 doi:10.1016/j.advwatres.2010.09.004, 2010.

882 Šimůnek, J., Angulo-Jaramillo, R., Schaap, M.G., Vandervaere, J.P., and van Genuchten, M.T.:
883 Using an inverse method to estimate the hydraulic properties of crusted soils from tension-disc
884 infiltrometer data. *Geoderma* 86(1): 61–81. doi: 10.1016/S0016-7061(98)00035-4, 1998.

885 Šimůnek, J., Sejna, M., Van Genuchten, M.T., Šimuunek, J., and Šejna, M.: HYDRUS-1D.
886 Simulating the one-dimensional movement of water, heat, and multiple solutes in variably-
887 saturated media, version 2, 1998.

888 Sisson, J., and van Genuchten, M.Th.: An improved analysis of gravity drainage experiments for
889 estimating the unsaturated soil hydraulic functions. *Water Resour. Res.* 27:569–575, 1991.

890 Singha, K., and Gorelick. S.M.: Saline tracer visualized with three-dimensional electrical
891 resistivity tomography: Field-scale spatial moment analysis. *Water Resources Research* 41(5).
892 <https://doi.org/10.1029/2004WR003460>, 2005.

893 Sposito, G.: *Scale Dependence and Scale Invariance in Hydrology*, Cambridge Univ. Press, New
894 York, <https://doi.org/10.1017/CBO9780511551864>, 1999.

895 Vanderborght J., and Vereecken, H.: Review of Dispersivities for Transport Modeling in Soils.
896 *Vadose Zone Journal* 6(1) doi:10.2136/vzj2006.0096, 2007.

897 Watson, K. K., 1966. An instantaneous profile method for determining the hydraulic conductivity
898 of unsaturated porous materials, *Water Resour. Res.*, 2, 709–715, 1966.

899 van Genuchten, M. T.: A closed-form equation for predicting the hydraulic conductivity of
900 unsaturated soils, *Soil Sci. Soc. Am. J.*, 44, 892–898, 1980.

901 van Genuchten, M.T., Leij, F.J. and Wu, L.: Characterization and measurement of the hydraulic
902 properties of unsaturated porous media (parts 1 and 2). *Proceedings of the International*
903 *Workshop, Riverside, Calif., 22--24 Oct, 1999.*

904 van't Veen, K. M., Ferré, T. P. A., Iversen, B. V., and Børgesen, C. D.: Using machine learning to
905 predict optimal electromagnetic induction instrument configurations for characterizing the
906 shallow subsurface, *Hydrol. Earth Syst. Sci.*, 26, 55–70, [https://doi.org/10.5194/hess-26-55-](https://doi.org/10.5194/hess-26-55-2022)
907 [2022](https://doi.org/10.5194/hess-26-55-2022), 2022.

908

- 909 Visconti, F., and de-Paz, J. M.: Sensitivity of soil electromagnetic induction measurements to
910 salinity, water content, clay, organic matter and bulk density. *Precision Agriculture*, 2021,1-19,
911 doi: 10.1007/s11119-021-09798-8, 2021.
- 912 von Hebel, C., Rudolph, S., Mester, A., Huisman, J. A., Kumbhar, P., Vereecken, H., and van der
913 Kruk, J.: Three-dimensional imaging of subsurface structural patterns using quantitative large-
914 scale multiconfiguration electromagnetic induction data, *Water Resour. Res.*, 50, 2732–2748,
915 <https://doi.org/10.1002/2013WR014864>, 2014.
- 916 von Hebel, C.; van der Kruk, J.; Huisman, J.A.; Mester, A.; Altdorff, D.; Endres, A.L.;
917 Zimmermann, E.; Garré, S.; Vereecken, H. Calibration, Conversion, and Quantitative Multi-
918 Layer Inversion of Multi-Coil Rigid-Boom Electromagnetic Induction Data. *Sensors* 2019, 19,
919 4753. <https://doi.org/10.3390/s19214753>.
- 920 Wang, X.-p., Quan, G.-j., Pan, Y.-x., Hu, R., Zhang, Y.-f., Tedeschi, A., Basile, A., Comegna, A.,
921 Coppola, A. and de Mascellis, R.: 2013. Comparison of hydraulic behavior of unvegetated and
922 vegetation-stabilized sand dunes in arid desert ecosystems. *Ecohydrol.*, 6: 264–274, 2013.
- 923 Wessolek, G., Plagge, R. Leij, F.J., and Van Genuchten, M.T.: Analysing problems in describing
924 field and laboratory measured soil hydraulic properties. *Geoderma* 64(1–2): 93–110.
925 [https://doi.org/10.1016/0016-7061\(94\)90091-4](https://doi.org/10.1016/0016-7061(94)90091-4), 1994.
- 926 Whalley, W. R., Binley, A. M., Watts, C. W., Shanahan, P., Dodd, I. C., Ober, E. S., Ashton, R.
927 W., Webster, C. P., White, R. P., and Hawkesford, M. J.: Methods to estimate changes in soil
928 water for phenotyping root activity in the field, *Plant Soil*, 415, 407–422.
929 <https://doi.org/10.1007/s11104-016-3161-1>, 2017.
- 930 Zare, E., Li, N., Khongnawang, T., Farzamian, M., and Triantafilis, J.: Identifying Potential
931 Leakage Zones in an Irrigation Supply Channel by Mapping Soil Properties Using
932 Electromagnetic Induction, Inversion Modelling and a Support Vector Machine, *Soil Syst.*, 4,
933 25, <https://doi.org/10.3390/soilsystems4020025>, 2020.
- 934 Zech, A., Attinger, S., Cvetkovic, V., Dagan, G., P. Dietrich, Fiori, A., Rubin, Y., Teutsch, G.: Is
935 unique scaling of aquifer macrodispersivity supported by field data? *Water resources research*
936 51(9): 7662–7679, <https://doi.org/10.1002/2015WR017220>, 2015.